



HAL
open science

Swirler effects on combustion instabilities analyzed with measured FDFs, injector impedances and damping rates

Preethi Rajendram Soundararajan, Daniel Durox, Antoine Renaud, Guillaume Vignat, Sébastien Candel

► To cite this version:

Preethi Rajendram Soundararajan, Daniel Durox, Antoine Renaud, Guillaume Vignat, Sébastien Candel. Swirler effects on combustion instabilities analyzed with measured FDFs, injector impedances and damping rates. *Combustion and Flame*, 2022, 238, pp.111947. 10.1016/j.combustflame.2021.111947 . hal-03570157v2

HAL Id: hal-03570157

<https://hal.science/hal-03570157v2>

Submitted on 25 Feb 2022

HAL is a multi-disciplinary open access archive for the deposit and dissemination of scientific research documents, whether they are published or not. The documents may come from teaching and research institutions in France or abroad, or from public or private research centers.

L'archive ouverte pluridisciplinaire **HAL**, est destinée au dépôt et à la diffusion de documents scientifiques de niveau recherche, publiés ou non, émanant des établissements d'enseignement et de recherche français ou étrangers, des laboratoires publics ou privés.

Swirler effects on combustion instabilities analyzed with measured FDFs, injector impedances and damping rates [†]

Preethi Rajendram Soundararajan^{*a}, Daniel Durox^a, Antoine Renaud^a, Guillaume Vignat^a, Sébastien Candel^a

^aLaboratoire EM2C, CNRS, CentraleSupélec, Université Paris-Saclay, 3 rue Joliot Curie, 91190 Gif-sur-Yvette, France

Abstract

The influence of the injection system on combustion instabilities is investigated on a laboratory-scale combustor equipped with a single injector that is weakly-transparent to acoustic waves. The combustor is fed with liquid heptane delivered as a spray by a hollow cone atomizer. Experiments are carried out with three swirlers having similar geometries but different pressure losses and swirl numbers. Self-sustained oscillations (SSOs) corresponding to these swirlers feature differences in oscillation frequency and amplitude for a given chamber length. These observations do not match with standard modeling predictions. Therefore, a low-order analytical model is derived, representing the effect of the acoustically weakly-transparent injection system using an impedance at the injector outlet. This quantity and the flame describing function (FDF), both determined experimentally, are used together with damping rate estimates as model inputs. It is shown that the FDF can only be determined by suitably selecting the position for the measurement of incident velocity disturbances at the injector outlet and that plenum-based velocity measurements cannot be used for this purpose. It is also assumed that the OH^{*}-chemiluminescence intensity can be used as a proxy for the heat release rate. This admittedly strong assumption for spray flames is discussed in detail and justified by showing that the equivalence ratio modulations are relatively weak for the particular spray flames considered in this study. Results from the model indicate that the injector impedance (that depends on the swirler characteristics) shifts the classical bands of instability and modifies the growth rate magnitude compared to a generic combustor with an acoustically transparent injector. Using the proposed model, the stability of the system can be rated along with a prediction for growth rate and frequency of oscillation. Predictions generally agree with experimental observations with some limitations. The model combined with damping rate estimates is finally used to predict limit cycle oscillation amplitudes with the aid of the FDF framework.

Keywords: Self-sustained combustion oscillation, spray-swirl combustor, flame describing function, injector dynamics, low-order modeling.

1. Introduction

Combustion instabilities often raise serious issues in the development and operation of high-performance devices such as liquid propellant rockets, aircraft engines, and gas turbines. Early work on rocket thrust chambers provided fundamental insights on the mechanisms driving and coupling combustion instabilities, emphasizing effects associated with the delay inherent to the combustion process and its sensitivity to the state variables [1, 2]. Considerable research carried out more recently in relation with novel combustor architectures for gas turbines has focused on the underlying mechanisms and control techniques, an effort reviewed for example by Candel [3], Huang and Yang [4], and Poinso [5]. In aeronautical engines and gas turbines for energy production, much of the research has been focused on configurations operating in

[†]Published version: <https://doi.org/10.1016/j.combustflame.2021.111947>

^{*}Corresponding author: Preethi Rajendram Soundararajan. *Email address:* preethi.rajendram-soundararajan@centralesupelec.fr

a nearly premixed mode, in which a swirling injector stabilizes the flame at a distance from the combustor backplane. These swirled injectors produce relatively compact flames, featuring a large volumetric power in an environment characterized by a reduced level of damping, thus making the system more susceptible to instabilities [5, 6]. The flow generated by such injectors exhibits complex fluid mechanics such as vortex breakdown, presence of precessing vortex core etc., raising additional challenges in understanding the instabilities of such configurations (as discussed, for example, in [7, 8] and in reviews by [4, 9, 10]). Some of these investigations indicate that the injection unit plays a vital role in determining the dynamics of the system and its propensity to instability. In the wide variety of injection configurations, one may try to distinguish swirling units in terms of characteristic parameters, the most obvious being the swirl number S and the pressure drop Δp or the pressure drop coefficient $\sigma = 2\Delta p/\rho_0 u_b^2$ (where ρ_0 is the density and u_b is the injector bulk velocity), in addition to other parameters like the Reynolds number or the turbulence intensity at the injector outlet. By comparing injectors featuring different swirl numbers and pressure losses, the present investigation intends to underline the role of the swirler in the process leading to self-sustained oscillations (SSOs).

At this stage, it is worth reviewing some previous investigations that specifically examine the effects of swirling injector parameters on combustion dynamics. One indication of the key role of the swirl number is provided by the large eddy simulation (LES) of a swirl-stabilized, lean premixed combustor reported by Stone and Menon [11]. An increase in this number (achieved by changing the premixer vane angle) from 0.56 to 0.84 results in a 50% reduction in the amplitude of acoustic pressure oscillations. Another LES study by Huang and Yang [12] focused on the effect of swirl on flame dynamics in a lean premixed swirl combustor, indicates that high swirl numbers lead preferentially to transverse acoustic oscillations, whereas longitudinal oscillations prevail at weak swirl levels. Swirl number effects are also illustrated in a study by Durox et al. [13], which uses an injector with continuously variable swirl numbers. Different flame topologies are observed and two types of instabilities are identified, a higher frequency instability—occurring for larger values of the swirl number featuring the highest acoustic pressure amplitudes and another instability coupled with the plenum at lower values of the swirl number. A more recent investigation by Kim [14] considers the instability mechanism in an industrial-scale lean premixed gas turbine combustor with a swirling injector. Two swirlers with swirl numbers 0.4 and 0.8 were tested at different chamber lengths. The normalized pressure amplitude, as well as the heat release rate fluctuations, were more intense in the higher swirl number case than at the low swirl number situation. These experimental results are somewhat at variance with those described by [11]. The fact that these investigations arrive at opposing conclusions may be interpreted as an indication that the instability mainly depends on the flame dynamics and its coupling with acoustics but not directly on the swirl number value.

The effect of injector head loss is comparatively less well documented. In general, the injector unit introduces a large change in the passage area, and this causes a notable decoupling of the upstream manifold, as shown by Schuller et al. [15]. This is characterized by an acoustic coupling index \mathcal{E} , based on the expansion ratio between the chamber and injection unit cross-sections and on the fresh and burned gas temperature ratio. A large expansion ratio is often caused by a small passage area inside the injector, inducing a high pressure drop. However, it is not easy to distinguish the direct effect of the index \mathcal{E} from that associated with head loss. Recent work by Vignat et al. [16] considers the effects of injector pressure loss on SSOs using a set of swirling spray injectors. These injectors have the same swirl number, ensuring nearly identical flame structures but different head losses. The instability map is derived over a wide range of operating conditions, and it is found that instability regimes change when the operating conditions are varied. This shows the notable influence of the pressure drop on the system stability and on the oscillation intensity and nature. In another study, Polifke et al. [17] investigated a pressure loss instability mechanism in a swirl-stabilized premixed burner. Experiments indicated that the onset of instability corresponded to a negative slope of pressure drop characteristics with respect to the mass flow rate. The experimental observations were supported by analytical representation based on a network model using acoustic transfer matrices leading to an instability criterion. Indications on the notable influence of the injection parameters are also derived from recent experiments on annular combustors, which are reviewed in [18]. The potential of using low-order models in representing complicated swirler geometries was explored, for instance, by Fischer et al. [19] using transfer matrices that were experimentally validated under cold flow conditions in a combustor

with a variable swirl number. The pressure loss coefficient was also modified by variably blocking the swirl generator. These investigations naturally encourage one to look for the applicability of low-order models even in complicated swirling geometries.

From this review, it appears that in swirl-stabilized flames, the injector defines the combustion dynamics of the system to a large extent. Changes in injector characteristics that vary the swirl number could alter the flow behavior resulting in a different flame shape. Variations in the pressure drop across the injector (leading to a change in the injector impedance) may alter the coupling between plenum and chamber, thus modifying the instability behavior. This forms the motivation for the present investigation. A single injector system is employed to understand the injector effect on combustion instabilities under longitudinal SSOs. The flame describing functions (FDFs) [20, 21] of the various units are determined and used in combination with a stability analysis framework that employs a measured impedance at the injector outlet to interpret the experimental data.

The present article is organized as follows. Section 2 describes the SICCA-Spray setup. Experimental data gathered in Section 3 illustrate differences in SSOs that may be observed in this combustor with the different swirlers. Section 4 highlights the issue of finding an optimal position for measuring the input velocity fluctuations at the swirling injector outlet for a proper determination of the flame describing function. FDF measurements are then reported. Sections 5 and 6 describe the impedance measurements at the injector outlet and the damping rate estimation respectively. These data are combined with a theoretical model developed in Section 7 to predict the occurrence of instabilities. Comparison of the model predictions with experimental data underlines the importance of including injector dynamics in the theoretical model for instability analysis.

2. Experimental setup

2.1. The SICCA-Spray test rig

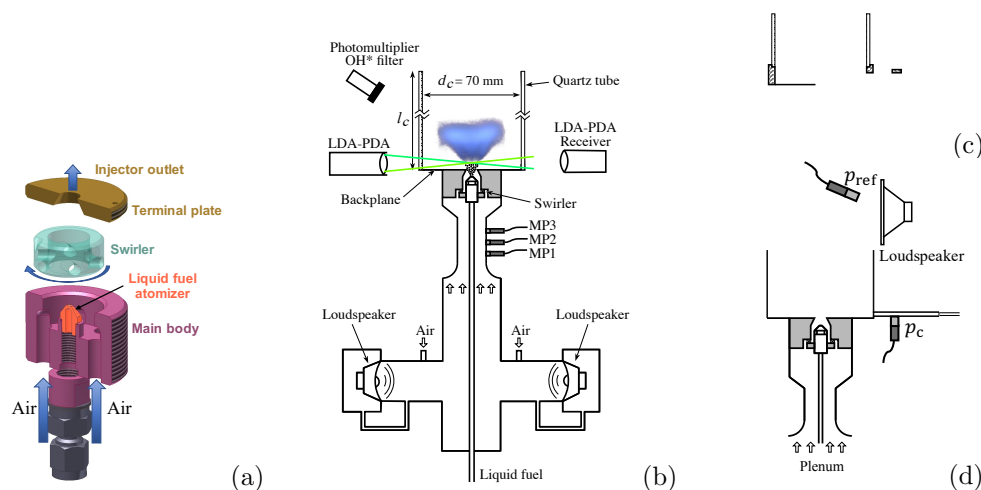


Figure 1: (a) Exploded view of the swirling injector showing its various components, adapted from [22]. (b) Schematic of the experimental setup of SICCA-Spray. The combustion chamber is configured for laser Doppler anemometry measurements. (c) Combustion chamber setup for pressure measurements during an SSO. (d) Schematic of the experimental setup used for damping measurements under cold flow conditions. The bottom portion of the plenum is not shown.

Experiments are carried out in a single injector setup (SICCA-Spray) representing one segment of the laboratory-scale annular combustor, MICCA-Spray [18]. The exploded view of the swirling injector is shown in Fig. 1a with its various components. The experimental setup shown schematically in Fig. 1b, comprises a

Table 1: Injector characteristics measured in an unconfined configuration (in cold flow) with a mass flow rate of $\dot{m}_{\text{air}} = 2.6 \text{ g s}^{-1}$. The swirl number S is measured at a height $h = 2.5 \text{ mm}$ above the outlet. The head loss coefficient is calculated using the equation $\Delta p = \frac{1}{2} \rho_0 \sigma u_b^2$ where u_b is the bulk velocity given by $\dot{m}_{\text{air}} / \pi \rho_0 R_{\text{inj}}^2$ and is equal to 43 m s^{-1} . Here $R_{\text{inj}} = 4 \text{ mm}$ is the radius of the injector outlet, d_{sc} is the diameter of the swirler channels and $2R_{0,sc}$ is the distance separating the axis of two opposing channels. Adapted from [22, 23].

Swirler	S (-)	Δp (kPa)	σ (-)	d_{sc} (mm)	$R_{0,sc}$ (mm)
707	0.60	3.65	3.33	4.0	4.6
712	0.59	4.50	4.10	3.0	2.3
716	0.70	5.74	5.23	3.5	4.7

plenum fed by air at atmospheric conditions by a Bronkhorst EL-FLOW mass flow controller with a relative accuracy of 0.6%. The plenum is connected to the combustor through a spray-swirl injector. The injector contains an air distributor leading to a tangential swirler with six channels [22]. The passage of air through the swirler channels induces a clockwise rotation of the incoming flow. The flow delivered by the swirler enters into the combustion chamber through a conical section with an 8 mm diameter outlet. Three swirlers are used in the current study, designated as 707, 712, and 716. The pressure drops Δp across the injector, the swirl numbers S , and the geometrical parameters of the swirlers (channel diameter d_{sc} and distance between the axis of two opposing channels $2R_{0,sc}$) are gathered in Tab. 1. The swirlers 707 and 712 have nearly the same swirl number and velocity profile at the outlet, but 712 has a higher pressure drop. The swirler 716 features a higher value for both swirl number and pressure drop. The swirl numbers are determined experimentally by integrating the velocity profiles at the injector outlet at a distance of 2.5 mm above that section. A detailed characterization of swirlers, velocity profiles, and droplet sprays may be found in [22, 23]. Liquid heptane fuel is supplied through a central tube in the plenum, and its mass flow rate is set by a Bronkhorst CORI-flow controller with a relative accuracy of 0.2%. The fuel is delivered as a hollow cone spray by a simplex atomizer producing a dispersion of fine fuel droplets. In the present study, the burner is operated at a global equivalence ratio of $\phi = 0.85$ and a thermal power of 6.4 kW, which corresponds to an air flow rate of 2.6 g s^{-1} and a fuel flow rate of 520 g h^{-1} .

Two types of combustion chambers are used depending on the measurement type (see Fig. 1b and 1c). In the configuration of Fig. 1b, velocity measurements near the injector outlet, flame visualization, and chemiluminescence intensity detection are carried out with a transparent quartz tube with an internal diameter of 70 mm and a length of 100 mm or 150 mm depending on the experiment. More details of the experimental conditions are given in Tab. 2. In a slightly different configuration, illustrated in Fig. 1c, a 15 mm-high metal ring is placed at the chamber bottom on top of which quartz tubes of different lengths are placed to complete the combustion chamber. The length of the chamber can thus be varied from 115 to 365 mm in steps of 50 mm, with an additional longest chamber of 465 mm. The bottom metal ring supports the water-cooled waveguide microphone MC1 (shown in Fig. 1c) that records the acoustic pressure close to the backplane. Two driver units mounted at the bottom of the plenum subject the system to external acoustic modulations for determining the flame response to incident velocity fluctuations at different perturbation amplitudes. The driver units are excited by a wave generator and a power amplifier.

2.2. Diagnostics

Three sensors (designated as MP1, MP2, MP3 in Fig. 1b) are installed in the plenum to measure pressure fluctuations at different positions. For the chamber pressure measurement close to the backplane, a microphone designated as MC1 is fixed on a water-cooled waveguide mounted on the bottom metal ring (Fig. 1c). The waveguide protects the sensor from the high-temperature environment in the chamber. It is formed by a straight metallic tube surrounded by a water jacket provided with a continuous circulation of cold water and terminated by a 25 m long tube to prevent possible wave reflection. The waveguide port is flush-mounted on the chamber wall and the microphone is placed on the waveguide at a distance of 276 mm,

resulting in a propagation delay of 0.79 ms in the acoustic pressure record. The sensors are Brüel & Kjær 4938 microphones mounted with type 2670 preamplifiers having a relative accuracy of 1% and a passband frequency set between 15 Hz and 20 kHz. The amplitude response of a microphone plugged on an infinite termination waveguide might differ from that of a microphone flush mounted on the wall, but the filtering imposed by the waveguide in the frequency range of interest remains weak. A study carried out in [24] (pp.119-122) with the same waveguide sensor, indicates that the amplitude is decreased by less than 8% at 1000 Hz. This deviation would be further reduced at lower frequencies of interest here (around 500 Hz) and one may, therefore, consider that the amplitude reduction is negligible. A photomultiplier fitted with an OH* filter (centered at 308 nm) detects the flame chemiluminescence $I(\text{OH}^*)$ emitted by OH* radicals. Additionally, an intensified CCD camera (PI-MAX from Princeton Instruments comprising 1024×1024 pixels) fitted with a Nikon 105 mm UV lens is used to visualize the flame shapes formed by each injection system by recording OH* light emission.

The velocity in the chamber is measured with a Dantec FlowExplorer 2-component phase Doppler anemometry (PDA) system, which is also used to measure the droplet size in the spray. The theoretical size of the laser beam intersection seen by the receiving optics is $0.14 \times 0.14 \times 0.23$ mm. The transmitting optics of this system has a focal length of 500 mm and the receiving optics has a focal length of 310 mm. The receiving optics is placed at 71.5° from the axis of the transmitting optics, an optimal position for particle size measurement for the heptane spray and for the small oil droplets which are used to seed the air flow when measuring under cold flow conditions. To have the best possible data rate, the velocity measurements are made with the system configured exclusively for anemometric measurements (laser Doppler anemometry—LDA). The system is operated in PDA mode only to get an estimate of the droplet size. In the measurements presented here, only the axial velocity component is measured, and for further information on radial and azimuthal components, the readers are referred to [22, 23]. All the chamber velocity measurements outlined in this study are carried out at 2.5 mm from the backplane of the chamber. For the cold flow measurements, the air flow is seeded with fine oil droplets while ensuring that their size is small enough to follow the flow well at frequencies up to 1000 Hz [25]. Table 2 gives a synthesis of the diagnostics used in the present experiments.

Table 2: Summary of the different experimental procedures described in this article. LDA: laser Doppler anemometry, SSO: self-sustained oscillation, FDF: flame describing function.

Experiment	Operation	Total chamber length	Measurement	Procedure	Section
Flame images	With flame Stable	100 mm	ICCD camera OH* chemiluminescence	Single image obtained by averaging 30 frames Abel deconvolution	3
SSO	With flame Stable/unstable	115, 165, 215, 265, 315, 365, 465 mm	Microphone MCI in chamber Mounted on bottom metal ring	Vary chamber length to obtain different SSO	3
Axial velocity profile	With & without flame Stable; acoustic forcing	100 mm	LDA Measurement of $u'_{c,r}/\bar{u}_{c,r}$	Upstream modulation at 700 Hz and $V_0 = 3$ V	4.1
FDF: Velocity	With flame Stable	150 mm	LDA Measurement of $u'_{c,r}/\bar{u}_{c,r}$	Upstream modulation: 300 Hz to 800 Hz $V_0 = 0.5$ V to 3 V $u'_{c,r}/\bar{u}_{c,r} = 0$ to 0.35	4.4
FDF: Heat release rate	Acoustic forcing		Photomultiplier OH* chemiluminescence		
Impedance under SSO	With flame Unstable	265, 315, 365 mm	Step 1: LDA - measurement of $u'_{c,r}/\bar{u}_{c,r}$ Step 2: Microphone MCI for chamber pressure	Chamber length varied to obtain SSO	5
Cold flow damping rate	Cold flow Stable; acoustic forcing	165 and 315 mm	Microphone MCI in chamber Measurement of frequency response	Downstream modulation: 300 Hz to 1000 Hz $V_0 = 5$ V	6.1

3. Self-sustained oscillations (SSOs)

Before describing the unstable operation, it is first interesting to examine flame images obtained under stable conditions with a chamber length of $l_c = 100$ mm. Figure 2 shows the OH* chemiluminescence images for the three different swirlers. A single image is obtained by averaging 30 frames and applying an Abel deconvolution. The flame shapes corresponding to the various swirler units are notably different especially near the central axis. For swirler 707, the flame is relatively narrow and takes a “V” shape. For swirler 712, the “V” shape opens up slightly, while for swirler 716, the flame spreads out and takes the form of a hollow “M” with a central trough, which may be attributed to the higher swirl induced by this swirler. From the

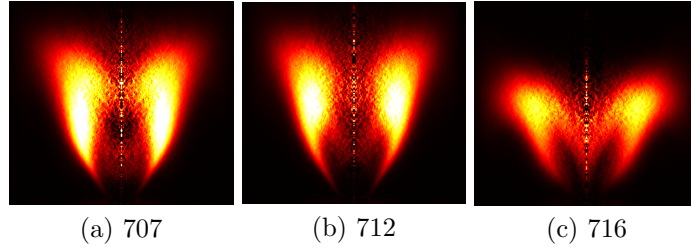


Figure 2: OH* images in SICCA-Spray for the three swirlers showing the flame chemiluminescence captured using an intensified CCD camera. The images are captured when SICCA-Spray is stable. An Abel deconvolution is applied to the average image recorded by the camera and is shown in false colors.

flame images, the axial location a_b of the heat release rate barycenter is estimated and it takes a value of 37 mm above the backplane for swirler 707, 38 mm for swirler 712, and 32 mm for swirler 716.

Instability characteristics are now examined during longitudinal self-sustained oscillations by varying the total chamber length l_c . This changes the eigenfrequency of the quarter-wave chamber mode and allows to investigate the influence of this parameter. Seven different chamber lengths are considered: 115, 165, 215, 265, 315, 365, and 465 mm and the pressure signals measured by MC1 are recorded at a sampling rate of $f_s = 16,384$ Hz for a total acquisition time of at least 8 s.

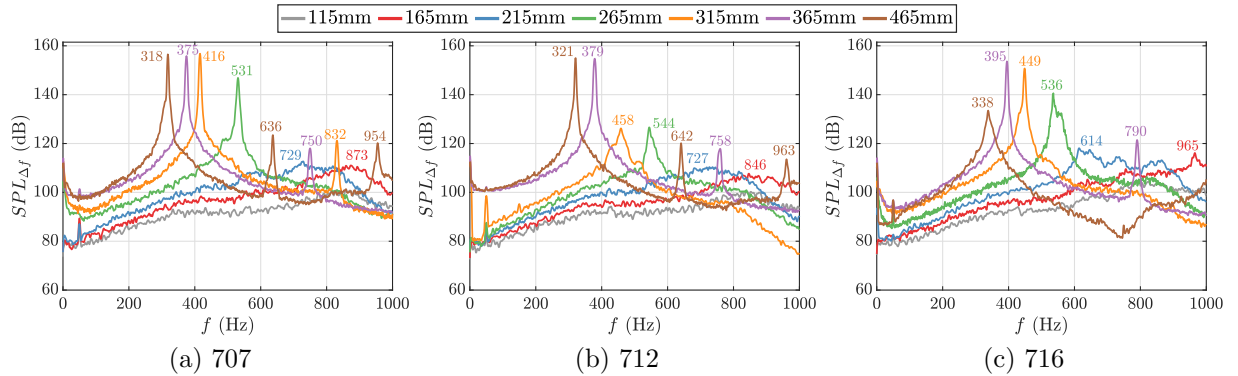


Figure 3: Frequency spectra showing the sound pressure level ($SPL_{\Delta f}$) measured by microphone MC1 near the combustor backplane for the three swirlers at different combustion chamber lengths l_c .

The pressure power spectrum of the signal from the chamber microphone MC1 is calculated using Welch's periodogram method, considering 32 Hamming windows with a 50% overlap between windows resulting in a frequency resolution of $\Delta f \approx 2$ Hz. The root mean square (RMS) of chamber pressure p_{rms} representing the instability amplitude (measured by MC1) and the peak frequency f_{peak} obtained from the frequency spectrum together characterize the self-sustained oscillations of SICCA-Spray. Figure 3 shows the power spectra plotted in terms of sound pressure level $SPL_{\Delta f}$ in the frequency band Δf and given in dB at different chamber lengths (the reference pressure being $p_{\text{ref}} = 2 \times 10^{-5}$ Pa). In the figure, the frequency corresponding to each peak is also marked.

At $l_c = 115$ mm, the spectra exhibit a relatively broadband shape without any prominent peak. The measured chamber pressure fluctuations are relatively low at this length, with a value of $p_{\text{rms}} = 67$ Pa for swirler 716, maximum among the three swirlers. SICCA-Spray is therefore considered to be stable at this length and $p_{\text{rms}}^{bl} = 67$ Pa is associated to background combustion and flow noise. This length with swirler 716 is considered as a baseline (*bl*) configuration for comparing the instabilities at other chamber lengths.

To determine whether the system can be considered stable or unstable, two criteria are used. A first condition to identify an unstable regime is that the pressure RMS value be at least twice that recorded

in the baseline configuration $p_{\text{rms}}^{\text{bl}} = 67 \text{ Pa}$, i.e. $p_{\text{rms}} > 2p_{\text{rms}}^{\text{bl}}$. In the second condition, the maximum $\text{SPL}_{\Delta f}$ in the spectrum (Fig. 3) is compared with the maximum $\text{SPL}_{\Delta f}^{\text{bl}}$ ($\approx 100 \text{ dB}$) recorded in the baseline configuration, and one requires that the maximum peak level exceeds the baseline level by a predetermined amount, typically $\Delta S = 30 \text{ dB}$. This condition may be written as $\text{SPL}_{\Delta f}(\text{peak}) > \text{SPL}_{\Delta f}^{\text{bl}}(\text{peak}) + \Delta S$. This criterion considers whether the system features a well-defined pure frequency tone. If the two conditions are met, one may say that the system is unstable, but when only one condition is met, the system is considered to be marginally unstable. An alternate criterion described in [26] was also examined for distinguishing stable and unstable points based on the probability density function (PDF) of time records of the pressure signal. Although this criterion results in an equivalent categorization for unstable and stable points, it classifies some marginally unstable points as stable even though a short but distinguishable peak is seen in the spectrum (e.g., 712 at $l_c = 265 \text{ mm}$ in Fig. 3).

Figure 4 shows the stability map of SICCA-Spray for the different chamber lengths based on the previous criteria. The peak frequency f_{peak} and pressure amplitude p_{rms} for the different chamber lengths are also shown in this figure. For swirler 707, at $l_c = 165$ and 215 mm , the system is stable as there is no peak in the frequency spectrum and p_{rms} is low. These points are represented as gray circles in Fig. 4. At the other lengths, SICCA-Spray with swirler 707 is unstable, marked by a prominent frequency peak and significantly higher values of pressure amplitude. This is denoted in the figure by red diamonds. With swirler 712, the system is stable at $l_c = 165$ and 215 mm , which can be seen from the lack of a peak in the frequency spectrum of Fig. 3b, and it exhibits a behavior similar to that of swirler 707 at this length. However, at $l_c = 265$ and 315 mm , SICCA-Spray is only marginally unstable, a behavior that differs from that of swirler 707 at these lengths. At $l_c = 365$ and 465 mm , the instability reaches a level similar but slightly lower to that of swirler 707. The instability frequency does not change between the swirlers 707 and 712 except during marginally unstable operation.

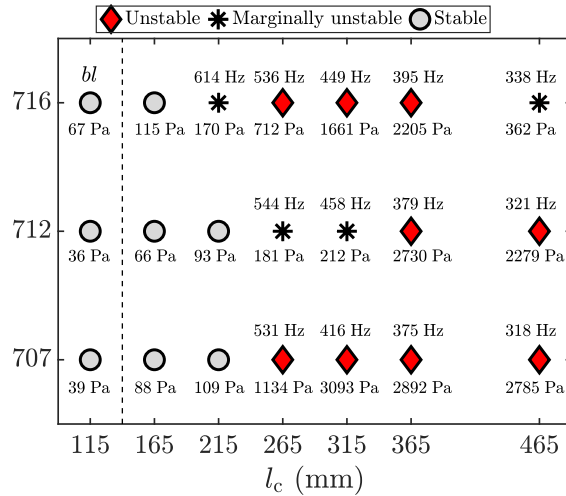


Figure 4: Experimentally determined stability map of SICCA-Spray under self-sustained oscillations at different chamber lengths l_c for the three swirlers. The peak frequency f_{peak} (Hz) from the frequency spectrum and RMS chamber pressure p_{rms} (Pa) measured by MC1 are indicated for each configuration. Gray circles correspond to stable points, black stars represent points that are marginally unstable, and red diamonds designate unstable points. The baseline level measured at $l_c = 115 \text{ mm}$ with swirler 716 is designated as *bl*.

For swirler 716, the only stable configuration is found at 165 mm apart from the baseline at $l_c = 115 \text{ mm}$. At $l_c = 215 \text{ mm}$, the system features a small peak in the frequency spectrum and the pressure amplitude p_{rms} is moderate. Consequently, SICCA-Spray is mildly unstable at this point—represented by a black star symbol in Fig. 4. At the lengths $l_c = 265, 315$ and 365 mm , SICCA-Spray is unstable with high chamber pressure amplitudes. However, when the length is increased further, 716 starts to enter the stable zone

and exhibits only a marginal instability at $l_c = 465$ mm. In general, swirler 716 has a lower oscillation amplitude during instability and also exhibits a difference in the oscillation frequency compared to the two other swirlers.

4. Flame describing functions (FDFs)

FDF measurements are performed by submitting the flame to different levels of acoustic velocity fluctuations induced by the loudspeakers located at the bottom of the plenum. The wave generator produces sinusoidal waves with an amplitude V_0 (peak to peak) of 0.5 V to 3 V in steps of 0.5 V and a linear frequency sweep is performed from 250 Hz to 850 Hz for a time duration of 133 s, at each level. This procedure subjects the flame to different levels of velocity modulation. The amplifier voltages given to the driver units are selected to produce a velocity fluctuation similar to the SSO measurements whenever possible. For the FDF measurements, it is necessary to ensure that SSOs are absent and that the system is stable. This is achieved by setting the chamber length at 150 mm.

In the absence of equivalence ratio fluctuation, the FDF is defined as the ratio of relative heat release rate (HRR) fluctuations to the relative volumetric flow rate fluctuations:

$$\mathcal{F}(\omega, \dot{q}'_v) = \frac{\dot{Q}'/\bar{Q}}{\dot{q}'_v/\bar{q}_v} \quad (1)$$

This formula corresponds to “the volume flow oscillations in the generation of excess flue gas volume due to thermal and combustion effects” according to “volume flow oscillations through the burner inlet port” [27, 28]. Here \dot{q}'_v is the volumetric flow rate; \dot{Q}' represents the fluctuation in HRR and \bar{Q} is the mean HRR³, both deduced from the light intensity of OH*. Further details on this measurement and its validity are given in Section 4.3.

In general, it is difficult to measure volume flow rate fluctuations whereas it is often easier to measure local velocity fluctuations at the outlet of an injector. The FDF is then determined from the equation [21]:

$$\mathcal{F}(\omega, |u'_{c,r}|) = \frac{\dot{Q}'/\bar{Q}}{u'_{c,r}/\bar{u}_{c,r}} = G_F(\omega, |u'_{c,r}|) e^{i\varphi_F(\omega, |u'_{c,r}|)} \quad (2)$$

Here, $G_F = |\mathcal{F}|$ and $\varphi_F = \arg(\mathcal{F})$ are the gain and phase of the FDF. $u'_{c,r}$ is the acoustic velocity fluctuation determined at the base of the flame (subscript ‘c’ referring to the measurement in the chamber) at a certain distance r from the center of the injector and at a particular height h from the chamber backplane. Equations (1) and (2) are equivalent if

$$\dot{q}'_v/\bar{q}_v = u'_{c,r}/\bar{u}_{c,r} \quad (3)$$

This equality is quite crucial in the measurement of the velocity reference for the FDF. Sections 4.1 and 4.2 focus on the choice of the measurement location to ensure that Eq. 3 is fulfilled. As will be seen in section 5 and Appendix C, with the type of injectors used in this study having a high pressure drop, the injector dynamics during SSO and acoustic forcing are not the same. It is then not advisable to use a reference velocity measured on the upstream side of the injector unit because this would lump the injector and flame dynamics. It is preferable to determine the FDFs by measuring the velocity at the base of the flame, where the equality of Eq. 3 is satisfied.

4.1. Axial velocity profiles

This subsection gives information about the spray and the velocity profile of swirler 716 as a reference case, both under cold flow and reacting conditions. A chamber length of 100 mm is used to avoid unwanted SSO.

³Here and henceforth the notation $(\cdot)'$ refers to fluctuations and $\overline{(\cdot)}$ refers to mean of a quantity.

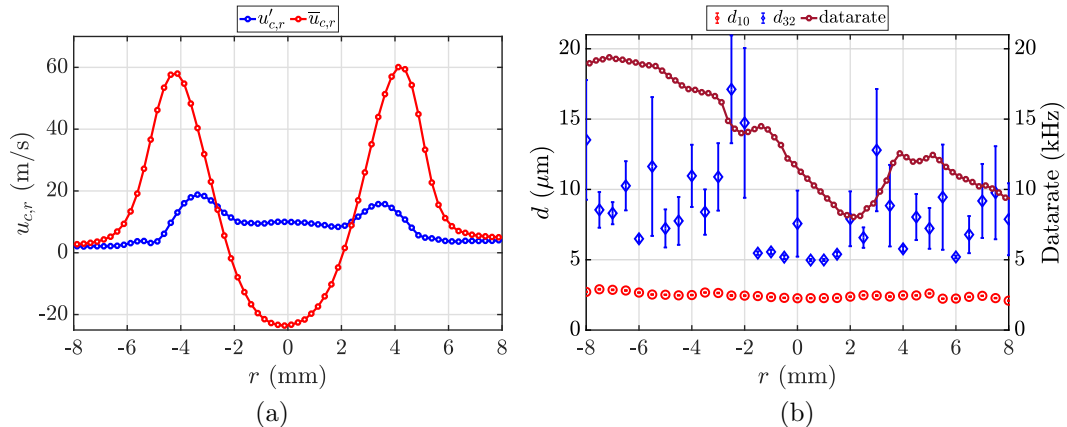


Figure 5: (a) Axial velocity profile measured in cold conditions showing mean (red) and RMS (blue) velocity fluctuations for swirler 716. The flow is seeded with small oil droplets and the system is pulsed at 700 Hz with an amplifier voltage $V_0 = 3$ V. (b) Mean (d_{10}) and Sauter mean diameter (d_{32}) of the oil droplets measured in PDA mode and the data rate of the measurement when operated under LDA mode. Error bars on the diameters indicate the statistics computed using bootstrapping method. All measurements are performed at a height of $h = 2.5$ mm above the chamber backplane.

Figure 5a shows the axial velocity profiles (mean and RMS) of 716 in the chamber when the cold flow is modulated at 700 Hz with an amplifier voltage of 3 V (peak to peak) applied to the SICCA-Spray driver units. The presence of a strong recirculation zone can be seen near the injector centerline, down to -20 m s^{-1} . The velocity reaches a maximum of 60 m s^{-1} at $r = 4$ mm. It is useful to note that the velocity fluctuation profile is not flat, and the maximum of the velocity fluctuation does not occur at the same radius as the maximum of the mean velocity. The data acquisition rate profiles and the mean diameter d_{10} and Sauter mean diameter d_{32} of the oil droplets are shown in Fig. 5b. The data rate quoted is for acquisition in LDA mode, while the droplet sizes are obtained in PDA mode. The large data rate allows reconstruction of the velocity signals up to 1000 Hz (more than 10,000 counts per second). Furthermore, d_{10} is small enough, of the order of 2.5 μm , for the oil droplets to follow the air flow well.

Under reactive conditions, the velocity measurements are made directly on the spray of heptane droplets. The mean and RMS velocity profiles for 716 are shown in Fig. 6a when the flame is modulated at 700 Hz with an amplifier voltage of 3 V (peak to peak). The maximum velocity is slightly higher than in cold flow (≈ 69 m s^{-1}) and occurs at $r = 4$ mm. The recirculation zone at the center of the injector is less pronounced than in the cold velocity profile (shown in Fig. 5a). This is because of fewer droplets in this region resulting in less precise velocity estimates. In Fig. 6b, the data acquisition rate and diameter profiles can be seen. It can be observed from the figure that beyond $r = 7$ mm there are practically no droplets due to the presence of flame front in this zone. The data rate is high between $r = 3$ mm to $r = 6$ mm (more than 20,000 counts per second), making it possible to temporally reconstruct the dynamics of the droplets. The particle sizes d_{10} and d_{32} change substantially depending on the position relative to the injector outlet (8 mm diameter). Close to the center, only a small amount of large droplets get trapped in the stagnation zone. As the atomizer produces a hollow cone, the fine droplets are ejected away from the axis. Outside the recirculation zone, from $r = 2.5$ mm, the droplet size is reduced, and the droplet number increases resulting in higher counting rate. Beyond the injector outlet radius, the particle size is augmented due to the spray impacting on the conical wall of the terminal plate and to the subsequent atomization of the liquid film formed in this process, a mechanism described in [22]. Just ahead of the injector outlet wall ($r = 4$ mm), the spray features very fine droplets ($d_{10} \approx 5$ μm) which can follow the air flow well even in the presence of strong velocity gradients. An estimate of the flow tracking by the 5 μm droplets can be done by simply looking at how they behave in a flow that is harmonically modulated. A classical calculation makes it possible to show that, with an oscillation at 500 Hz, the amplitude of the droplet velocity fluctuation is 95% compared to the

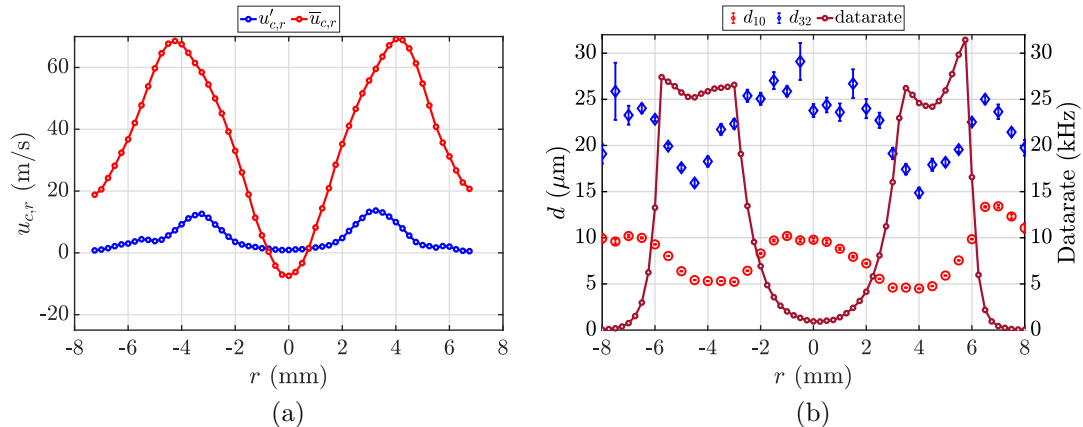


Figure 6: (a) Axial velocity profile measured in reactive conditions showing mean (red) and RMS (blue) velocity fluctuations for swirler 716. The system is pulsed at 700 Hz with an amplifier voltage $V_0 = 3$ V. (b) Mean (d_{10} in red) and Sauter mean diameter (d_{32} in blue) of the heptane droplets measured in PDA mode and the data rate of the measurement when operated under LDA mode. Error bars on the diameters indicate the statistics computed using bootstrapping method. All measurements are performed at a height of $h = 2.5$ mm above the chamber backplane.

amplitude of the gas flow. The delay remains low, of the order of $\pi/20$ for this droplet size and frequency. It is, therefore, possible to measure the relative velocity fluctuations that are needed to determine the FDF under reactive conditions by deducing the air velocity from the velocity measurement carried out on the fuel droplets in the region where the diameter d_{10} is small. It is pointed out in advance that the measurements made with the three swirlers under the same flow conditions give the values d_{10} of $5.4 \mu\text{m}$ for swirler 707 ($r = 3.5$ mm), $5.8 \mu\text{m}$ ($r = 3.5$ mm) for swirler 712, and $4.5 \mu\text{m}$ for swirler 716 ($r = 4$ mm). The reason for the droplet size measurements at these particular radii is given in the following section.

4.2. Location of velocity measurement in the chamber

The measurement of velocity fluctuations must be carried out at a point at the injector outlet, where Eq. 3 holds. However, in an arrangement comprising a swirler, the choice of this location is not straightforward due to the presence of strong velocity gradients at the injector outlet (see Figs. 5a and 6a). To verify Eq. 3, the mean \bar{q}_v and RMS \bar{q}'_v of volume flow rate fluctuations at the modulation frequency are acquired by integrating the measured velocity (from LDA) obtained under cold flow conditions at $h = 2.5$ mm (shown in Fig. 5a). The velocity is measured under cold flow conditions as the data rate under reactive conditions is too low in the central injection region, reducing the accuracy in this region. This measurement is carried out with the three swirlers: 707, 712, and 716 at three excitation frequencies: 300, 500 and 700 Hz and at an amplifier voltage of 3 V (applied to the two driver units). Only the results obtained with the swirler 716 and at 700 Hz are presented in this article as the conclusions remain the same at the other frequencies and for other swirlers. Details on the calculation of volumetric flow rate are provided in Appendix A. The radial evolution of $u'_{c,r}/\bar{u}_{c,r}$ for swirler 716 is shown in Fig. 7 along with the calculated \bar{q}'_v/\bar{q}_v . The curve of $u'_{c,r}/\bar{u}_{c,r}$ intersects the line of \bar{q}'_v/\bar{q}_v at four points: close to ± 4 mm and at ± 5 mm. It was previously shown that the diameter d_{10} of the spray droplets becomes larger beyond the injector outlet radius (Fig. 6b). It is therefore suitable to choose the point $r = \pm 4$ mm and $h = 2.5$ mm for the relative velocity fluctuation measurements to use in the FDF determination as it satisfies the equality in Eq. 3. The location of r for FDF determination plays a crucial role as even a 1 mm shift from the optimal position will result in a large difference (a factor of 2) between the rate of velocity fluctuation and the rate of volumetric flow fluctuation, with an error of the order of $\pi/10$ for the phase (see Appendix A). For example, a measurement carried out in the middle of the exit radius at $r = 2$ mm and at $h = 2.5$ mm would have dramatic consequences on the FDF estimation, both on the gain and on the phase. It can also be seen from Fig. 5a that this

location essentially corresponds to the maximum of the mean axial velocity. Although these measurements were performed under cold flow conditions, on comparing with the velocity profile with flame in Fig. 6a, one finds that the maximum of mean axial velocity still occurs at $r = \pm 4$ mm, validating the usage of cold flow conditions for selecting the measurement location of the relative velocity fluctuation used in the FDF. For the swirlers 707 and 712, the same measurement and subsequent calculations resulted in the optimum position to be at $h = 2.5$ mm and $r = 3.5$ mm, corresponding to the position of maximum mean axial velocity.

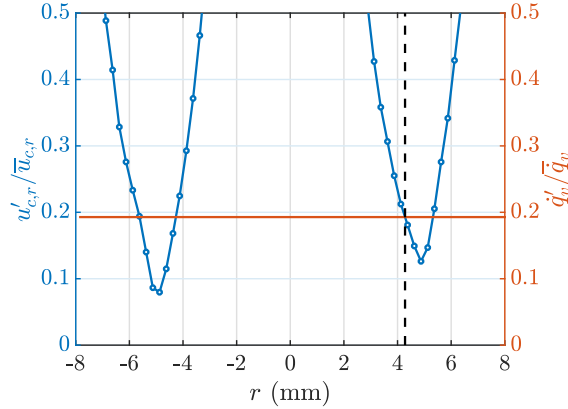


Figure 7: Ratio of RMS to mean velocity at different radii and the calculated volume flow rate. The vertical dotted line in black shows the location where relative velocity fluctuations coincide with the relative volume flow rate fluctuations. These measurements are made under cold conditions with oil seeding and by pulsing the system at 700 Hz and $V_0 = 3$ V. The measurements are performed at a height of $h = 2.5$ mm above the chamber backplane. The results close to the center of the injector are not shown as the $u'_{c,r}/\bar{u}_{c,r}$ values are high due to the low value of $\bar{u}_{c,r}$ and also as the region of interest for this figure lies close to the injector outlet radius.

4.3. Heat release rate determination

The determination of the unsteady heat release rate (HRR) is of pivotal importance in combustion dynamics analysis and specifically for the determination of FDFs (Eq. 2). This quantity is often deduced from the chemiluminescence emission intensity of excited radicals like OH^* or CH^* . The relation between this signal and the HRR is well established for lean premixed flames [29, 30] but less well documented in the case of spray flames. One indication of the light intensity $I(\text{OH}^*)$ being monotonically linked to the HRR in case of a spray flame is provided by [31]. The light emission is found to be quasi-linearly related to the integrated HRR \dot{Q} over the flame volume. This has been confirmed recently by [23] based on systematic steady-state experiments carried out in the SICCA-Spray burner. As the fuel flow rate is varied, the light intensities of OH^* or CH^* are found to increase monotonically with the mass flow rate of fuel \dot{m}_f and only weakly deviate from a linear dependency. The deviation from linearity is also found to be less significant in the case of OH^* chemiluminescence than CH^* chemiluminescence [23]. A second issue that needs to be considered is the possibility of equivalence ratio fluctuations that might arise when the spray flame is modulated. Such a fluctuation would mean that using OH^* chemiluminescence for determining HRR fluctuation might not be appropriate for estimating the FDF defined in Eq. 2, which only considers fluctuations in velocity. The fuel side impedance defined by a pressure atomizer is stiff, thereby fixing the mass flow rate of fuel. But the air flow rate fluctuates in response to pressure disturbances in the chamber, generating fluctuations in the equivalence ratio. However, in the present case, it is found that a strong fluctuation of the air mass flow rate causes only weak fluctuations of the equivalence ratio. Further confirmations of this point are given in Appendix B by analyzing the variation in the $(I(\text{CH}^*)/I(\text{OH}^*)) / (I(\text{CH}^*)/I(\text{OH}^*))$ ratio, which can be

linked to the equivalence ratio in hydrocarbon flames [32, 33, 34, 35] and specifically verified for a fluctuating lean spray-flame in [36]. In the appendix, it is shown that this ratio measured with two photomultipliers features a low amplitude ripple during a cycle of oscillation which has the same order of magnitude in both a fully premixed situation and in the spray flame case. It is worth noting that the ratio of instantaneous intensities is scaled by the ratio of mean intensities so that the gains of the two photomultipliers do not intervene. Additionally, images of the ratio $I(\text{CH}^*)/I(\text{OH}^*)$ are obtained with an intensified CCD camera to verify the presence of any spatial inhomogeneities of equivalence ratio in the flame. These images, sampled during an acoustic oscillation cycle, show that there is no apparent stratification of equivalence ratio in the flame zone. The variations in equivalence ratio measured by this technique remain relatively low ($< 5\%$ at the maximum of flow rate fluctuation, which is of the order of 25% for swirler 716). This ability of the injector to premix the fuel spray well with air is due to the recessed position of the atomizer in the injector (Fig. 1a and b) and high volatility of the fuel used. The atomizer outlet is located at a distance of 6.75 mm upstream of the injector outlet in a converging nozzle (marked as terminal plate in Fig. 1a). Part of the spray, which comes out from the hollow cone atomizer, impacts the converging conical section of the nozzle before exiting the injector. When the air flow fluctuates, it causes the fuel spray to fluctuate inside the nozzle. Hence, at the injector outlet, the fuel flow rate is also modulated in phase with the air flow rate fluctuations. The equivalence ratio fluctuations therefore remain low at the injector outlet. This phenomenon is analogous to what was observed in [36] for a kerosene spray flame, where the atomizer is also located well inside the injector and surrounded by preheated air. Additionally, it is shown in [37], through comparison of purely acoustic and chemiluminescence measurements, that even for a technically premixed flame with equivalence ratio fluctuations, the phase evolution of OH^* fits well with the phase of HRR. More details on this point are provided in Appendix B. Thus, based on the arguments presented above, it can be reasonably concluded that, in the present study, the light intensity $I(\text{OH}^*)$ is indicative of \dot{Q}' in the flames.

4.4. Results

It is now worth examining the FDF corresponding to the three swirlers operating under the same conditions ($\mathcal{P} = 6.4\text{ kW}$ & $\phi = 0.85$) as the self-sustained instabilities. The FDFs shown in Fig. 8 represent the variation of gain G_F and phase φ_F with frequency for different values of velocity fluctuation level in the chamber, $u'_{c,r}/\bar{u}_{c,r}$. For the FDF calculation, the signals recorded from the photomultiplier (measuring the HRR) and the velocity signals delivered by LDA are filtered $\pm 5\%$ around the signal generator frequency. The velocity RMS is determined by integrating the power spectral density of the filtered signal. The transfer function between the filtered HRR and velocity fluctuations is obtained by dividing the cross power spectral density of these two signals by the spectral density of the relative velocity signal. The spectral densities are estimated using Welch's periodogram method. Each frequency block of two seconds in the ramp is divided into 8 Hamming windows with a 50% overlap between windows. The measurements are performed in the frequency range between 300 Hz and 800 Hz. The low frequency range below 300 Hz is not covered because of the limitations of the modulation system of driver units. This situation is often found in similar investigations (see for example [38]). Additionally, FDF measurements below 300 Hz are outside the range of interest for the current study.

In general, the three FDFs have similar shapes, but one also notices significant variations. This is particularly the case for the gain curves (Fig. 8 left). The position of the maximum gain is around 520 Hz for swirler 712 and around 600 Hz for swirler 716. For swirler 707, the gain is nearly flat up to 600 Hz after which it begins to fall. The gain only weakly changes with the input level for swirlers 707 and 712, while it is more sensitive to this level for swirler 716. Thus, swirlers 707 and 712 are still in the linear regime with respect to the input, while the behavior of the flame formed by swirler 716 is nonlinear in the vicinity of the gain maximum, i.e., around $f = 600$ Hz. The phase evolution (Fig. 8 right) is quasi-linear with frequency. The slopes corresponding to the different swirlers are of the same order of magnitude, but with some variations in the delays that may be deduced from these slopes. These delays are 1.32, 1.53 and 1.48 ms for swirlers 707, 712 and 716 respectively. Assuming that the delay is essentially controlled by convection, one may deduce from these delays the length scale a from the injector outlet where the heat release fluctuations take place. Considering that the perturbations travel at half the maximum of the mean

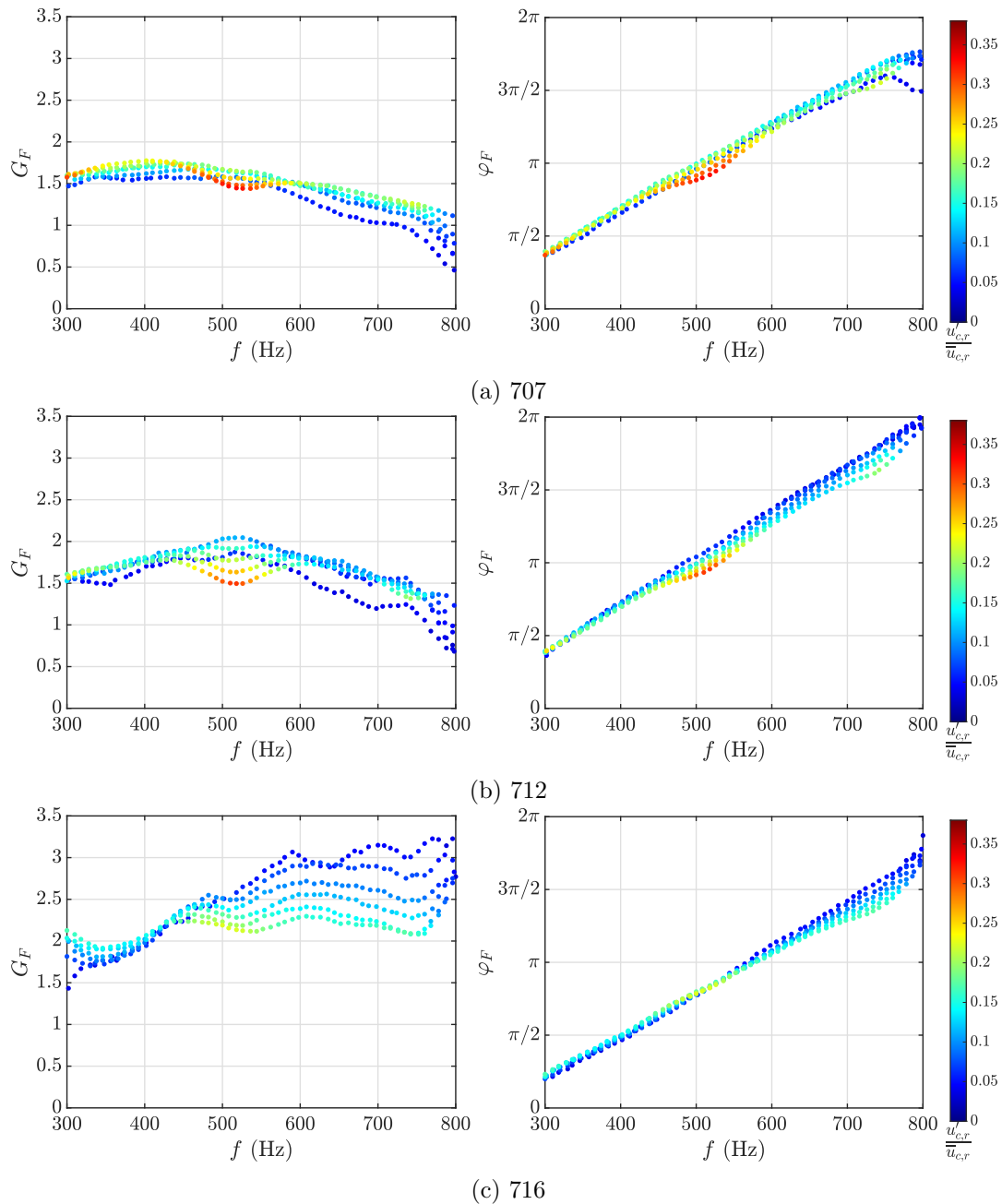


Figure 8: Flame describing function gain G_F (left) and phase φ_F (right) for the three swirlers. From top to bottom: swirlers 707, 712, and 716. The color scale represents the level of velocity fluctuations measured at $r = 3.5$ mm for swirlers 707 and 712, and $r = 4$ mm for swirler 716, at a height of $h = 2.5$ mm from the backplane. Here, $u'_{c,r}$ and $\bar{u}_{c,r}$ are respectively the RMS velocity fluctuations and mean velocity fluctuations ('c' refers to measurements made in the chamber and 'r' refers to the radius at which the velocity fluctuations are measured). The data are smoothed using a five-point moving average.

velocity on the axial velocity profile [39] (maximum velocity is around 69 m s^{-1} for swirler 716 shown in Fig. 6a, 58 m s^{-1} for swirler 707 and 56 m s^{-1} for swirler 712—not shown), one obtains for a : 3.8, 4.3 and

5 cm respectively for swirlers 707, 712 and 716. This distance is slightly longer than the axial distance of the heat release rate barycenter a_b determined in Section 3.2 under stable conditions, but is only approximate. Even if the delay is relatively precise, the estimate of the mean convection velocity is less accurate. As the distance a_b is known more precisely, it will be used in the theoretical model described in Section 7. It is worth noting that this distance has only a minor impact on the results.

5. Impedance at the injector outlet during a self-sustained oscillation

Changing the injector does not only change the dynamic behavior of the flame, as indicated in the previous section but also modifies the acoustic response of this unit. For low-order models, it is difficult to consider the entire system with the complicated upstream geometry. This can be simplified by modeling only the chamber with an impedance at the inlet representing the combined response of the injection unit and upstream manifold. In a previous numerical study ([40], pp. 144-158), it was observed that the injector dynamics is not the same during an upstream acoustic modulation and SSO. This means that, for the same amplitude of velocity fluctuation downstream of the injector, the velocity fluctuations upstream of the swirler, in the plenum, is completely different between SSO and forcing. This observation is confirmed experimentally with the sensors located upstream (MP1, MP2, and MP3) and downstream of the injector (MC1 and LDA) during the acoustic forcing and SSO experiments (shown in Appendix C). Such behavior could be attributed to the strong pressure drop created by the small air channels in the swirler, resulting in strong acoustic decoupling of the upstream (plenum) and downstream (combustion chamber) cavities. To have an impedance that is representative of the injector and the upstream cavity during an SSO, it is, therefore, necessary to modulate the system from downstream (unlike the FDF measurement in Section 4 where the system is modulated from upstream). Even though such a downstream modulation is carried out for damping measurements described in the next section, it is not possible to do this with flame in the SICCA-Spray test rig. However, the impedance may be directly measured during an SSO, where there is a strong pressure oscillation downstream, and this is done in two steps here. Firstly, during an SSO, the velocity fluctuation $u_{c,r}$ at the outlet of the injector is measured with LDA. Next, the pressure fluctuation p'_c close to the backplane is recorded with the waveguide microphone MC1. The two measurements cannot be performed simultaneously because MC1 is supported on a metal ring comprising the water-cooled waveguide, and this blocks the optical access required for the LDA measurements. From the pressure and velocity measurements, the specific impedance $\zeta = p'_c/(\rho_u c_u u'_{c,r})$ at the outlet of the injector is calculated for the three swirlers. The density ρ_u and the speed of sound c_u are considered at a temperature of the fresh stream of air ($T_u = 293$ K). It is verified that the OH* signal is the same between the two measurements, and this serves as a phase reference to deduce the phase difference between pressure and velocity.

Figure 9 shows the specific impedance for the three swirlers at different instability frequencies—in other words, for different combustion chamber lengths. Only the impedance corresponding to a limit cycle oscillation with sufficient amplitude is shown in the figure. The phase of specific impedance takes similar values for the swirlers 707 and 712, and its value is close to $3\pi/4$, especially when the instability is high (i.e., for longer chamber lengths and therefore for lower frequencies). For swirler 716, this phase is closer to π when the amplitude of instability is highest (i.e., at the chamber length $l_c = 365$ mm and for a frequency of 395 Hz). A quasi-phase opposition between pressure and velocity at the injector outlet has also been observed previously in LES calculations of an annular system exhibiting combustion oscillations [41] and more recently in [42] under downstream transverse acoustic field with similar type of injector as those in the present work. This effect arises when the acoustic pressure amplitude downstream of the injector exceeds the mean dynamic pressure of the flow [43, 44] and is analogous to the injection-coupling analyzed in the domain of combustion instabilities in rocket engines [45]. The impedance values reported here will be used in the theoretical framework described in Section 7. Growth rates obtained from this theoretical model will be compared to damping rates determined in the following section.

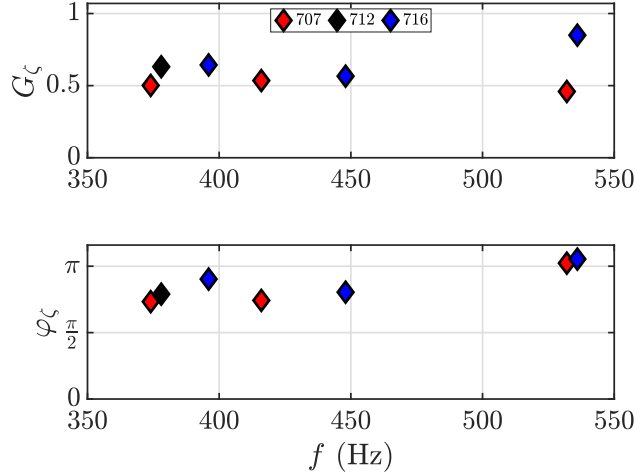


Figure 9: The modulus G_ζ and phase φ_ζ of the injector impedance for the three swirlers. The measurements are reported only under limit cycle self-sustained oscillations at different frequencies.

6. Damping rate estimate

To determine the stability of the system, it is essential to know the damping rate induced by each swirler. Two methods for the experimental determination of the damping rate are exploited in this section. In the first, one assumes that the system behaves like a second-order linear system and the damping rate is deduced from the half-power bandwidth Δf_r of the resonance curve. This measurement can, however, only be performed in cold flow conditions. In the second method, the damping rate is estimated from an energy balance during a limit cycle oscillation.

6.1. Cold flow damping rate estimation using the resonance curve method

Performing this measurement in cold flow conditions is admittedly a limitation of this procedure, but it is still instructive to have an estimate of the changes in damping rate that may be linked with the different swirlers.

The experimental setup for this measurement is shown in Fig. 1d. A driver unit placed near the top of the combustor excites the system and the pressure response (p_c) is measured with microphone MC1. During this measurement, the two bottom loudspeakers are left electrically open, as they are during the self-sustained instability experiments. A microphone located in front of the driver unit serves as a reference and measures the frequency response p_{ref} of this device. The combustor surroundings are covered with an acoustic liner to reduce unwanted reflections. The measurement of damping is performed at two chamber lengths in cold condition (with $\dot{m}_{\text{air}} = 2.6 \text{ g s}^{-1}$), $l_c = 165 \text{ mm}$ and $l_c = 315 \text{ mm}$, such that the resonance response occurs around the frequency of SSO in SICCA-Spray. At $l_c = 165 \text{ mm}$, the chamber resonates at a frequency $f_{\text{chamber}} \approx 460 \text{ Hz}$ corresponding to a quarter wave mode while at $l_c = 315 \text{ mm}$ it resonates at $f_{\text{chamber}} \approx 760 \text{ Hz}$, corresponding to a three quarter wave mode of the chamber. A frequency sweep is performed around the resonance frequencies at a ramp rate of 1 Hz s^{-1} . The measurements are sampled at a frequency of $f_s = 16,384 \text{ Hz}$ and measured in blocks that are 2 s long. Damping is deduced from $\alpha = \pi \Delta f_r$, where Δf_r is the width of the resonance curve at half power. The calculation of frequency response is performed using Welch's periodogram technique by averaging two Hamming windows at each 1 s block with 50% overlap. This results in a frequency resolution of $\pm 1 \text{ Hz}$ which in turn corresponds to a damping uncertainty of $\pm 3.14 \text{ s}^{-1}$. The calculated damping values are indicated in the top row of Fig. 10b at 460 Hz and in the bottom row for 760 Hz. The damping rate is found to be about 90 s^{-1} at 460 Hz and 120 s^{-1} at 760 Hz, with some variation between the swirlers. The lowest value corresponds to the swirler 712 at both frequencies. It is interesting to note that the swirler geometry influences this damping rate and that the variation in damping is of about 20% of the mean level at 460 Hz whereas such a difference

between swirlers is less evident at 760 Hz. However, these measurements do not quite represent the level of damping corresponding to the system under hot fire conditions. In particular, there is no temperature evolution between the upstream manifold, injector, and chamber. This will modify the resonance conditions and the mode shape. The cold flow measurements only provide an estimate of the level of damping that may be expected for this system and to distinguish the swirlers in terms of their damping rate.

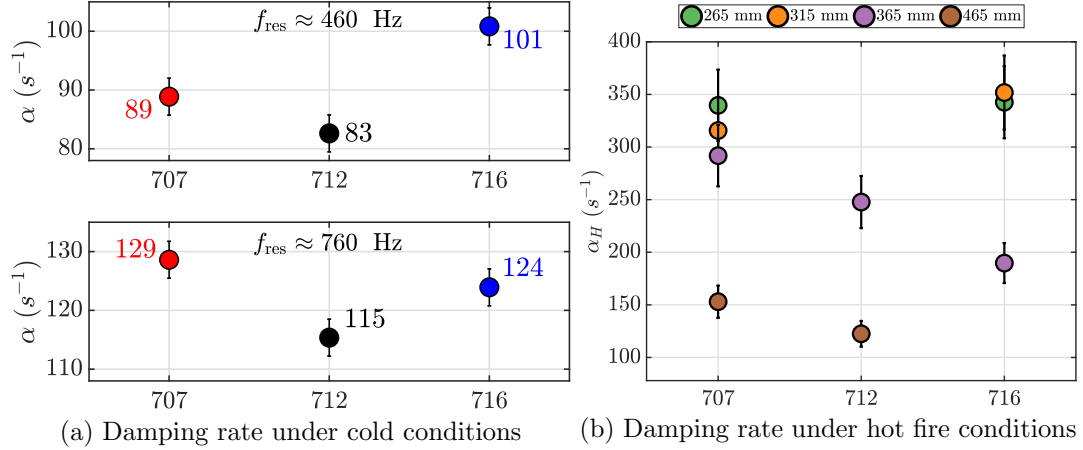


Figure 10: (a) The top row shows the damping ($\alpha = \pi \Delta f_r$) for the three swirlers at a frequency of 460 Hz with a chamber length of 165 mm. The bottom row shows damping at 760 Hz measured with a chamber length of 315 mm. The error bars indicate the uncertainty in damping, which is determined from the frequency resolution in Welch’s periodogram calculation and is equal to ± 1 Hz. (b) Damping rate under hot fire conditions deduced using energy balance method. The error bars represent an approximate uncertainty which is considered to be about 10%. The damping rate estimate is obtained only from measurements corresponding to a well-established limit cycle oscillation.

6.2. Hot fire damping rate estimation using energy balance method

It is not easy to obtain a direct measurement of the damping rate when there is a flame. For example, it is not possible to perform a downstream modulation as the hot gases might damage the driver unit located close to the chamber exit and the combustion noise will hamper in obtaining a noise-free resonance curve. Furthermore, it is not possible to cover the surroundings with liner material because of the hot exhaust stream. One may instead use a system identification method or an acoustic energy balance. These two methods were exploited in [23] (pp.245-255) in the case of axial coupling in the annular configuration MICCA-Spray equipped with the same swirling injectors (of the 716 type). It was found that the damping coefficient was $\xi \simeq 6 \times 10^{-2}$ giving a damping rate under hot fire conditions $\alpha_H = \xi \omega_0 \simeq 170 \text{ s}^{-1}$.

The acoustic energy balance method is used in the present configuration and the damping rate obtained with this method is given by:

$$\alpha_H = \frac{\langle S \rangle}{2 \langle E \rangle} \quad (4)$$

where α_H refers to the damping rate under hot fire conditions, $\langle S \rangle$ is the volume integrated Rayleigh source term, $\langle E \rangle$ is the acoustic energy density integrated over the volume. This equation is valid only when the oscillations have reached a limit cycle. The individual expressions for $\langle S \rangle$ and $\langle E \rangle$ along with their derivation are given in [23, 46] and are not provided here. After few calculations one may finally express the damping rate in terms of spectral densities as:

$$\alpha_H = (\gamma - 1) \frac{Re(S_{p'} \dot{Q}')}{S_{p'p'} V} \quad (5)$$

where $S_{p',\dot{Q}'}$ is the cross power spectral density between chamber pressure and heat release rate, $S_{p'p'}$ is the power spectral density of the chamber pressure, both obtained at the fundamental frequency of a limit cycle oscillation, and V is the chamber volume. This expression is used to obtain the damping rate using the experimentally obtained SSO described in Section 3. Results are shown in Fig. 10b for the different swirlers at various lengths. The uncertainty in this damping estimate is not well known but is approximately considered to be about 10% (indicated by error bars). This does not preclude the analysis that will be carried out in the upcoming section, and it may be treated as a means to incorporate the variability that characterizes the experimental measurements of damping rates. The damping rate under hot conditions is two to three times larger than the damping rate under cold flow operation. The changes observed are partially linked to the variations in resonance frequency. As this method is valid only for a limit cycle oscillation, damping rate cannot be obtained for oscillations corresponding to a marginal instability (for example, at $l_c = 265$ and 365 mm for swirler 712 and at $l_c = 215$ and 465 mm for swirler 716).

7. Low-order theoretical model

A simplified theoretical analysis is now carried out to help understand the self-sustained instability observations and devise a model for instability prediction. This can be done, for instance, by defining unstable bands in the FDF phase diagram using linear stability analysis. Conventionally, to determine these bands, one could choose a simple model with three cavities to represent the combustor—with a plenum, an acoustically transparent injector, and a combustion chamber open to the atmosphere. This is exemplified in [47], in which case, the unstable bands for the first axial mode correspond to $\pi < \varphi_F < 2\pi, \text{ mod}[2\pi]$. If the first of these bands is considered with swirler 716 for example (see Fig. 8c right), then the possible unstable frequencies would only lie between 580 Hz and 880 Hz and this is at variance with the observed oscillation frequencies which are much lower (400 Hz to 530 Hz as shown in Fig. 4). As mentioned before, these injectors exhibit a relatively high pressure drop, and they do not exhibit the same dynamics with an upstream acoustic modulation or during an SSO, where there is a strong pressure oscillation downstream. Thus, these injectors are weakly transparent to acoustic waves and it is necessary to consider the acoustic response of the injector in terms of an impedance at its outlet to suitably propose a low-order model. Thus, a simple model with two cavities is considered—one representing the injector outlet and the other representing the combustion chamber open to the atmosphere.

7.1. Model formulation

This modeling effort relies on a compact flame representation, with the flame represented as a plane discontinuity in combination with a one dimensional acoustic model of wave propagation, an open boundary condition at the combustor exhaust, and an effective specific impedance ζ at the injector outlet. The system is sketched in an idealized manner in Fig. 11b. Here, the injector is represented by a short cylindrical tube of length 1 mm and an experimentally measured impedance at the injector outlet representing the upstream manifold. The short length of the injector corresponds to the straight cylindrical section of the terminal plate (shown in Fig. 1a), just after the conical convergent nozzle (highlighted by the red ellipse in Fig. 11a). This short section has an outlet diameter of $d_1 = 8$ mm leading to the combustion chamber, with an inner diameter of $d_2 = 70$ mm. The flame is located at a distance a_b from the chamber backplane and this corresponds to the location of the flame barycenter calculated from the flame images in Fig. 2. The jump conditions relating pressure and velocity at the different sections of this idealized configuration are derived by making use of the standard convention where the time harmonic term in all waves is $\exp(-i\omega t)$. The acoustic pressure and velocity can be represented as follows:

$$p'_j(x, t) = A_j \exp(ik_j x - i\omega t) + B_j \exp(-ik_j x - i\omega t) \quad (6)$$

$$u'_j(x, t) = \frac{1}{\rho_j c_j} [A_j \exp(ik_j x - i\omega t) - B_j \exp(-ik_j x - i\omega t)] \quad (7)$$

A_j and B_j correspond to the amplitudes of the waves, $k_j = \omega/c_j$ is the acoustic wavenumber, ρ_j and c_j are respectively the density and speed of sound in the j^{th} section and ω designates the angular frequency. In

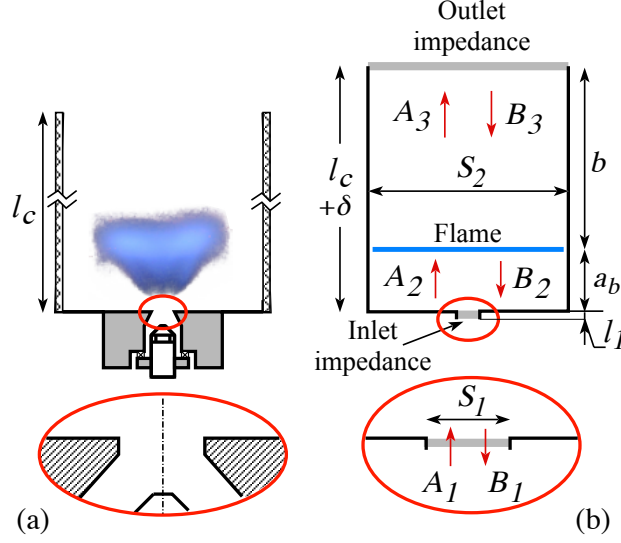


Figure 11: Model representation of the combustion chamber. (a) Real configuration, (b) Idealized model. The injector and upstream manifold are replaced by an effective impedance at the injector outlet. An end correction δ is used to account for acoustic radiation from the combustor outlet.

section 1 the specific impedance at the injector outlet and the jump condition for pressure and volumetric flow rate perturbations give:

$$A_1 e^{ik_1 l_1} (1 - \zeta) + B_1 e^{-ik_1 l_1} (1 + \zeta) = 0 \quad (8)$$

$$A_1 e^{ik_1 l_1} + B_1 e^{-ik_1 l_1} - A_2 - B_2 = 0 \quad (9)$$

$$A_1 \frac{S_1}{\rho_1 c_1} e^{ik_1 l_1} - B_1 \frac{S_1}{\rho_1 c_1} e^{-ik_1 l_1} - A_2 \frac{S_2}{\rho_2 c_2} + B_2 \frac{S_2}{\rho_2 c_2} = 0 \quad (10)$$

The jump condition across the flame deduced from the linearized Rankine-Hugoniot relation yields [47],

$$S_2 u'_3 - S_2 u'_2 = \frac{\gamma - 1}{\rho_0 c_0^2} \dot{Q}' \quad (11)$$

Here, S_2 is the cross-sectional area at the flame location, which is the same upstream and downstream of the flame. \dot{Q}' is the HRR and can be represented by the FDF. It is recalled here that the velocity reference for the FDF measurement is that existing at the injector outlet and using Eq. 2 one finds,

$$S_2 u'_3 - S_2 u'_2 = \frac{\gamma - 1}{\rho_0 c_0^2} G_F e^{i\varphi_F} \bar{Q} \frac{u'_1}{u_1} \quad (12)$$

Here, u_1 is the velocity measured close to section 1 and is the same as $u_{c,r}$ in Eq. 2. G_F and φ_F represent the gain and phase of FDF respectively. The mean HRR from the flame can be represented in terms of burnt products and incoming fresh reactants temperatures (T_b and T_u respectively) and is given by $\bar{Q} = \dot{m} \bar{c}_p (T_b - T_u)$. $\dot{m} = \rho_1 S_1 u_b$ is the total mass flow rate and u_b is the bulk velocity at the injector outlet. Specific heat coefficient is $\bar{c}_p = \frac{1}{T_b - T_u} \int_{T_u}^{T_b} c_p dT = \frac{\dot{m}_f}{\dot{m}} \frac{\Delta h}{T_b - T_u}$ where \dot{m}_f represents the mass flow rate of heptane and Δh is the lower calorific value of heptane equal to 44.6 MJ kg^{-1} . $\rho_0 c_0^2 = \gamma \bar{p}$ is nearly constant across the flame region. Here, \bar{p} represents the mean pressure and it is suitable to consider that $\rho_0 c_0^2 = \rho_1 c_1^2 = \rho_1 \gamma r T_1$. Eq. 11 can be further simplified as,

$$S_2 u'_3 - S_2 u'_2 = \Theta F \Gamma S_1 u'_1 \quad (13)$$

Here $\Theta = (T_b/T_u) - 1$ is the volumetric expansion parameter and Γ is \bar{c}_p/c_p . It is next convenient to replace $\Theta\mathcal{F}$ by $\hat{\mathcal{F}}$. In this simplified 1D case, u_b and \bar{u}_1 cannot be differentiated although they are different. Here, u_b is replaced by \bar{u}_1 and this is valid as long as Eq. 3 is satisfied.

Now, imposing a continuity condition for the pressure fluctuation across the flame yields,

$$A_2 e^{ik_2 a_b} + B_2 e^{-ik_2 a_b} - A_3 - B_3 = 0 \quad (14)$$

Considering an open end at section 3,

$$A_3 e^{ik_3 b} + B_3 e^{-ik_3 b} = 0 \quad (15)$$

Here $b = l_c + \delta - a_b$ where l_c is the chamber length and $\delta \approx 0.4 \times d_2$ is the acoustic end correction [48, 49]. Eqns. 8, 9, 10, 13, 14 and 15 are combined to obtain a set of linear equations in the form $M \times X = 0$, where $X = [A_1 \ B_1 \ A_2 \ B_2 \ A_3 \ B_3]^T$ and M is

$$\begin{bmatrix} e^{ik_1 l_1} (1 - \zeta) & e^{-ik_1 l_1} (1 + \zeta) & 0 & 0 & 0 & 0 \\ e^{ik_1 l_1} & e^{-ik_1 l_1} & -1 & -1 & 0 & 0 \\ \frac{S_1}{\rho_1 c_1} e^{ik_1 l_1} & \frac{-S_1}{\rho_1 c_1} e^{-ik_1 l_1} & \frac{-S_2}{\rho_2 c_2} & \frac{S_2}{\rho_2 c_2} & 0 & 0 \\ \frac{\hat{\mathcal{F}}\Gamma S_1}{\rho_1 c_1} & \frac{-\hat{\mathcal{F}}\Gamma S_1}{\rho_1 c_1} & \frac{S_2}{\rho_2 c_2} e^{ik_2 a_b} & \frac{-S_2}{\rho_2 c_2} e^{-ik_2 a_b} & \frac{-S_2}{\rho_3 c_3} & \frac{S_2}{\rho_3 c_3} \\ 0 & 0 & e^{ik_2 a_b} & e^{-ik_2 a_b} & -1 & -1 \\ 0 & 0 & 0 & 0 & e^{ik_3 b} & e^{-ik_3 b} \end{bmatrix}$$

On solving for the nontrivial solution of M which requires that $\det[M] = 0$, one obtains the dispersion relation of this system:

$$\begin{aligned} \frac{S_1}{\rho_1 c_1 \rho_3 c_3} \cos(k_3 b) \sin(k_2 a_b) + \frac{\hat{\mathcal{F}}\Gamma S_1}{\rho_1 c_1 \rho_2 c_2} \sin(k_3 b) + \frac{S_1}{\rho_1 c_1 \rho_2 c_2} \cos(k_2 a_b) \sin(k_3 b) \\ - \frac{i\zeta S_2}{\rho_2 c_2 \rho_3 c_3} \cos(k_2 a_b) \cos(k_3 b) + \frac{i\zeta S_2}{\rho_2^2 c_2^2} \sin(k_2 a_b) \sin(k_3 b) = 0 \end{aligned} \quad (16)$$

The complex roots of this expression $\omega = \omega_r + i\omega_i$ can be obtained by numerically solving the dispersion relation. The frequency of oscillation is deduced from $\omega_r = 2\pi f$ while ω_i provides the growth rate. The values of ρ and c in each section correspond to the following temperatures $T_1 = 293$ K, $T_2 = 573$ K, and $T_3 = 900$ K. The value of T_3 here is much lower than the burnt gas temperature $T_b = 2100$ K as the former value is an estimation of mean temperature in the chamber. This was approximately determined in a steady state experiment by coating the inner wall of the quartz tube with a thermochromic paint (MC153-14 from TMCHallcrest adapted to a temperature range of 160 to 1240 °C).

7.2. Model predictions

A necessary condition for instability is that the growth rate be positive, i.e., $\omega_i > 0$. This defines an instability band that is shown in gray in Figs. 12 and 13. In addition to this, it is also necessary that the growth rate exceeds the damping rate to sustain an instability. Solving Eq. 16 provides this growth rate and the expected oscillation frequency but it requires two parameters as input, the gain and phase of the FDF, which depend on frequency. Therefore an iterative process is used to solve the dispersion relation until convergence is reached on the predicted frequency. The experimentally measured FDFs shown in Section 4 display a dependence on the velocity fluctuation level $u'_{c,r}/\bar{u}_{c,r}$ in addition to the frequency, which adds

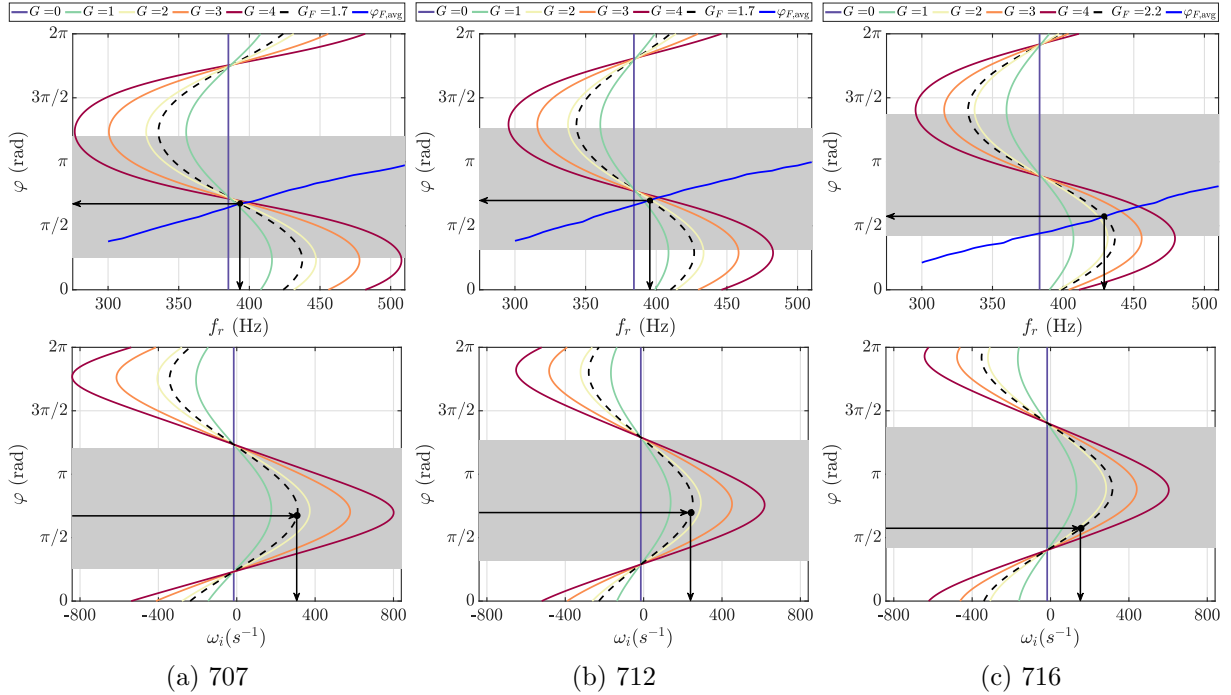


Figure 12: Frequency and growth rate prediction from the model for different gains and phases at $l_c = 365$ mm. The unstable band is defined when $\omega_i > 0$ and indicated by the gray bands. The dotted black curve corresponds to the final gain of FDF G_F and the black dot is the point where it intersects the final phase ($\varphi_{F,\text{avg}}$). The converged frequency and growth rate prediction are obtained at this point. The arrows show the direction of obtaining a value from the graphical solution.

more complexity to obtaining the solution. Hence for simplicity, the dispersion relation is solved using a flame transfer function framework (without taking the fluctuation level into account), as a first step. For this purpose, FDF gain and phase values shown in Fig. 8 are averaged over the fluctuation level at each frequency (obtaining $G_{F,\text{avg}}$ and $\varphi_{F,\text{avg}}$).

Figure 12 shows the roots of the dispersion relation when gain G and phase φ are taken as independent parameters (not measured) for a chamber length $l_c = 365$ mm for the three swirlers. It also graphically illustrates the procedure to solve the dispersion relation. Firstly, one chooses an arbitrary value for the gain, say $G=1$ (green curves on the top row of Fig. 12), and plots the roots of the dispersion relation as a function of an arbitrary phase φ . The intersection with the curve $\varphi_{F,\text{avg}}(f_r)$ (blue curve in the top row of Fig. 12) then gives an initial value of oscillation frequency f_r (represented by the downward arrow in Fig. 12). This frequency is then used to obtain a new gain from the transfer function (averaged FDFs) and the dispersion relation is solved to obtain a new oscillation frequency. The above process is repeated until convergence on the oscillation frequency is reached. The final gain (dotted black curve in Fig. 12) and phase at this converged frequency is used to obtain the growth rate (bottom row in Fig. 12 indicated with a downward arrow).

One may now compare the model predictions with the observations of SSOs. This is done in Figs. 13 and 14. Two conditions need to be satisfied for instability to occur. In the first, the predicted point should fall inside the instability band. The growth rate then is positive so that the system will be potentially unstable. In addition, the predicted growth rate must exceed the damping rate. Figure 13 compares the calculated instability bands with results from experiments to verify the first condition. The symbols represent experimental SSO data from Section 3. The frequencies correspond to the peaks of the spectra in Fig. 3 and the phase $\varphi_{F,\text{avg}}$ is obtained using an average of the FDF phase plots from Fig. 8, shown as blue dotted lines.

For each of these experimental data points, the instability band for the corresponding length and swirler is obtained by solving the dispersion relation and shown in gray. The position of the unstable band notably depends on the injector impedance and, more specifically, on its phase φ_ζ . The band location substantially differs from the standard position corresponding to a quarter wave mode coupling $[\pi, 2\pi]$ ([47, 50]). When the experimental data point falls within the instability band (as is the case for the three swirlers at $l_c = 365$ mm), the model predicts a positive growth rate, and the system is potentially unstable. Conversely, when the point falls outside the instability band, the model predicts a negative growth rate and the system will be stable. It can be seen that the predictions are mostly confirmed by experiments since all unstable points fall well within the predicted instability bands. It is also instructive to compare the instability bands with the evolution of the phase curve. For example, the model predicts that swirler 716 is unconditionally stable for any frequency below 375 Hz and that swirler 712 is also unconditionally stable above 600 Hz. In Fig. 13, the dark gray bands with black outline represent the points where the impedance is experimentally measured (definite prediction). For the points where the impedance is not measured, the nearest neighbor value is used to obtain the solution and the predicted unstable band is shown with a lighter shade of gray (approximate prediction). This procedure is admittedly a limitation, but if the frequency is close enough, the impedance might be expected not to vary much.

As mentioned earlier, a positive growth rate only indicates a potential instability but is not enough to predict whether the system is effectively unstable. For this purpose, one must check if the predicted growth rate is higher than the damping rates determined in Section 6. Figure 14 reports the predicted instability frequencies and growth rates for all investigated cases. Points that fall outside the instability bands are marked as stable. Points that fall within the instability band, but for which the damping rate is unavailable or is higher than the predicted growth rate are dubbed “potentially unstable”. The former ones are the points that correspond to a marginal instability in SSO (refer Fig. 4) and where the hot fire damping rate cannot be obtained. Points that fall inside the band and for which the growth rate exceeds the estimated damping rate are unstable. Note that in Fig. 13, the symbols correspond to the experiments, whereas, in Fig. 14, they correspond to the prediction from the model. On comparing the predicted stability map with the experimental stability map (Fig. 4), one can see that the model predicts all the stable and most of the unstable operations. It can be seen from Fig. 14 that the growth rate exceeds the damping rate (typically of the order of 150 to 350 s⁻¹), indicating the growth of oscillations at most unstable points, except two (712 at 465 mm and 716 at 365 mm). However, the growth rate at these points is still fairly close to the

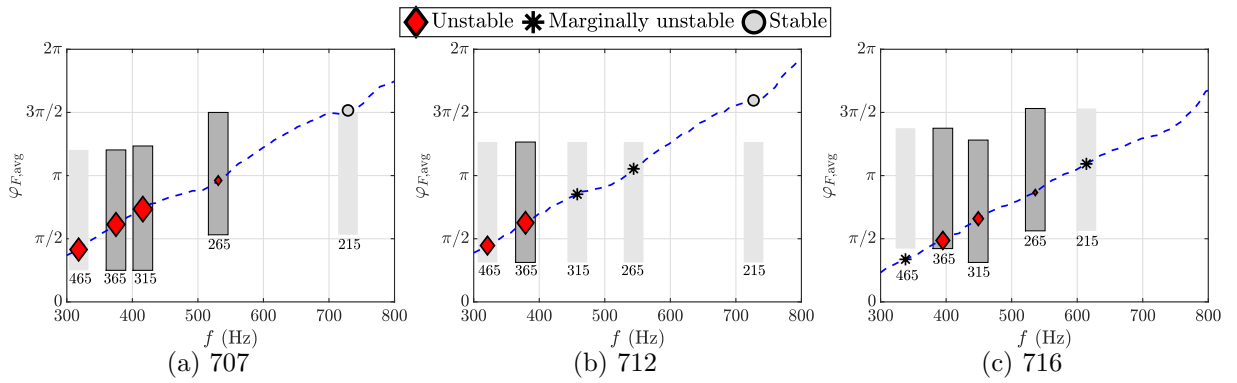


Figure 13: Instability bands (marked in gray) predicted by the model are shown at self-sustained oscillation (SSO) frequency for the three swirlers. The combustion chamber length l_c is quoted under each band in mm. The dark gray bands with black outlines correspond to a definite prediction and the light gray bands refer to an approximate prediction. For the unstable points (black diamonds with red shading), the size of the marker is proportional to the RMS chamber pressure p_{rms} . The blue dotted line represents the phase of the FDF averaged over the fluctuation level $\varphi_{F,avg}$. The theoretical model provides unstable bands while the FDF phase and the stability of the system are obtained from experiments (also shown in Fig. 4).

lower limit of the damping rate. The marginally unstable points from the experiments cannot be predicted accurately, and only a potential instability can be speculated. The lack of experimental impedance and definite damping rate estimate and an analysis based on a linear approach can contribute to the inexact prediction of such points. At the two smaller lengths (115 mm and 165 mm) experimental FDF data are not available beyond 800 Hz to make an exact prediction. However, if one linearly extrapolates the phase, the resonant frequencies that can be expected for these two lengths in hot conditions would lie outside the band giving a stable prediction. The frequency predicted by the model is close but almost always has a difference of ± 20 Hz compared to the experimental measurement of SSO.

In the method described here, an average gain and phase of FDF is considered to remove the dependence on the fluctuation level. This iterative process can also be extended to deal with the dependence of FDF on the input level $u'_{c,r}/\bar{u}_{c,r}$ and is exemplified in Section 7.3 for the swirler 716.

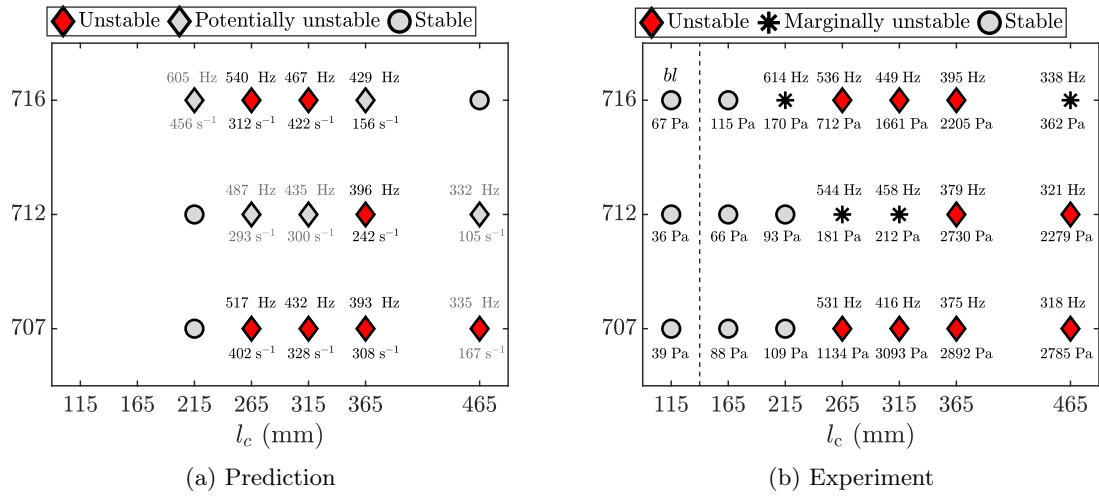


Figure 14: (a) Prediction obtained from the model at different chamber lengths l_c . The predicted frequency and growth rate are indicated when the prediction points to an unstable operation. Black font colors are marked to show a definite prediction from the model, whereas gray font colors show only an approximate prediction. The gray circles represent the stable points, gray diamonds represent the potentially unstable points, and red diamonds represent the unstable points. (b) Experimentally obtained stability map duplicated from Fig. 4.

7.3. Model prediction at different u'/\bar{u}

The theoretical model to consider the measured FDF at different u'/\bar{u} (same as $u'_{c,r}/\bar{u}_{c,r}$ in Section 4) for limit cycle prediction is demonstrated here. The process consists in applying the iteration procedure presented in Section 7.2 for every input level u'/\bar{u} of the FDF. One can then predict the growth rate and frequency of oscillation as a function of the input level. These two quantities are plotted in Fig. 15 for the swirler 716 at two chamber lengths $l_c = 265$ and 315 mm. Swirler 716 is chosen as its FDF exhibits sufficient difference with respect to the input level, whereas, for swirlers 707 and 712, considering an average FDF is still reasonable as the FDFs do not vary much with respect to the input level in the available data range. Figure 15 shows the changes in growth rate ω_i in the top row as the relative velocity fluctuation level is augmented. These figures also indicate the level of damping α_H (shown as a band to represent uncertainties) under hot fire conditions that were estimated in Section 6. A limit cycle oscillation may be expected when $\omega_i \simeq \alpha_H$. For a chamber length $l_c = 265$ mm, the limit cycle corresponding to this condition implies a level of velocity fluctuation u'/\bar{u} that is of the order of 0.1. On comparing with the experimental measurement at this length, $(u'/\bar{u})_{SSO} \approx 0.06$ which is close to the predicted oscillation level. For $l_c = 315$

mm, the crossing point between ω_i and α_H is slightly outside the range where the FDF was measured, but the value of u'/\bar{u} may be extrapolated and is 0.32. In comparison with the measurements, the fluctuation level is $(u'/\bar{u})_{SSO} \approx 0.14$, which is much lower than the prediction. While the predicted frequency is close to that found experimentally, the predicted level of velocity oscillation is twice that observed during SSO. This discrepancy could be attributed to the linear extrapolation of u'/\bar{u} which might not be adequate.

Using the predicted fluctuation level, one may try to estimate the frequency at limit cycle, the evolution of which is shown in the bottom row of Fig. 15. The frequencies at limit cycle are predicted to be $f_{LC} = 540$ and 453 Hz respectively at $l_c = 265$ and 315 mm which agree with the experimental values of 536 and 449 Hz (refer Fig. 4 or Fig. 14b).

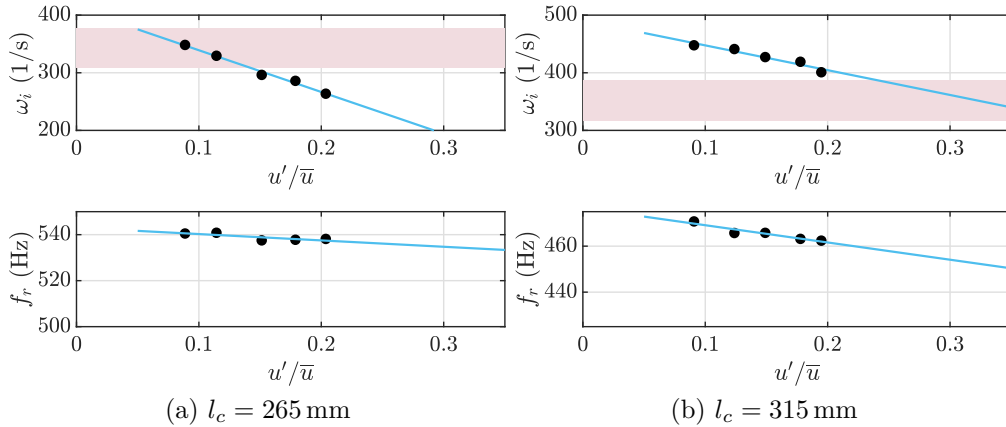


Figure 15: Prediction of growth rate and frequency at different u'/\bar{u} for swirler 716. The red band shows the calculated damping under hot fire conditions α_H described in Section 6 with an uncertainty of 10%. The black circles indicate the prediction by the model at different u'/\bar{u} while the solid blue line shows a linear fit applied to these points.

7.4. Model implications

Figure 13 reveals that the position of the unstable band changes with the swirler and with the combustion chamber length (in other words, with the instability frequency). This is because the unstable bands are solely determined by the phase φ_ζ imposed by the injector impedance at the entrance of the combustion chamber and this changes with the swirler and frequency. The impedance modulus G_ζ determines the growth rate magnitude. A smaller impedance modulus results in a broader evolution of growth rate and frequency with respect to the phase of the FDF. On revisiting the question raised at the beginning of the section on why the standard instability band of $\pi < \varphi_F < 2\pi$ does not work for the instability prediction in the present case, it can be seen that this is due to the changes in phase imposed by the injector unit between the pressure and local velocity disturbances. The instability band of $\pi < \varphi_F < 2\pi$ works if the velocity is in quadrature with respect to the pressure i.e. $\varphi(u', p') = 3\pi/2$ as considered in [51]. But such a band cannot be used for modeling the injectors considered in the present study because these elements define impedance at the combustion chamber inlet that do not correspond to such a quadrature. It is then important to have a good model for the injector impedance or to use an experimentally determined impedance. The injectors used in this study are not acoustically transparent resulting in a certain degree of decoupling between plenum and chamber. Such decoupling has been observed in a previous study with these injectors on the annular test rig MICCA-Spray [52], where the observed instability is mainly a chamber mode decoupled from the plenum.

The injector outlet impedance is deduced from measurements during SSO in this work. This is not completely satisfactory since, logically, it would be necessary to use a measurement that is independent of the SSO. One could use a downstream modulation of the flame in the frequency band of interest by measuring pressure near the chamber backplane and velocity fluctuations at the outlet. This kind of modulation was not feasible in the present experimental setup. Despite this limitation in the experimentation, the knowledge

of impedance derived from SSO, even at discrete frequencies, allows a good prediction of the instability bands and, therefore, validates the modeling strategy. It is also seen that the impedance does not vary much with the type of swirler and the frequency of oscillation. For all the tests carried out in this study the modulus of the impedance is of the order of 0.5, and the phase is between $3\pi/4$ and π . With an injector roughly identical to those in the present study, and with a downstream modulation by acoustic waves transverse to the flame, Patat et al. [42] obtain similar phase shift values. Alternatively, a simple theoretical analysis of the behavior of injectors with significant pressure drops can be done to estimate the impedance phase. It is possible to consider that the injector operates in the quasi-steady regime. The calculations show that the real part of the impedance is negative and generally larger than the imaginary part. One may then express $\zeta = \zeta_r + i\zeta_i$ with $\zeta_r = -\kappa\bar{u}\sigma/c$. In this expression, σ designates the head loss parameter and κ is a coefficient of the order of one. It is less easy to obtain an expression for ζ_i but it is possible to infer from the data that $|\zeta_i| \ll |\zeta_r|$ so that the phase angle φ_ζ is generally close to π .

The experimental measurements presented here and the subsequent modeling approach feature certain limitations. For example, the measurement of impedance is performed in two steps: one with a metal ring to measure pressure signals and the other with a quartz chamber to obtain velocity fluctuations. This sort of approach might change the thermal environment at the flame base, resulting in a small error in the measured impedance. This induces some uncertainties, especially near the limits of the unstable band. The model also uses a linear approach that cannot distinguish marginally unstable points. The other limitation is in the prediction of limit cycle amplitude. Even though an estimate of hot fire damping was obtained with the energy balance method, there exists an uncertainty in this estimation, making it difficult to predict the oscillation amplitude at the limit cycle. There is also a limitation of the modulation system to reach a fluctuation level (u'/\bar{u}) similar to those found at the limit cycle. As a consequence, the FDF data do not cover the full range of relative velocity fluctuations that may arise in the system. Although the present modeling has limitations, it nevertheless highlights the importance of injector impedance on the instability of the system calling for studies aimed at identifying the role of injector dynamics and modeling injector impedance.

8. Conclusion

Experiments and theoretical modeling reported in this article underline the importance of the injection unit in combustion instability analysis. The present investigation considers seven combustion chamber lengths and three different swirlers with a fixed geometry of the upstream manifold and the injector unit. Experiments are conducted under the same operating conditions with liquid heptane as fuel delivered as a spray by a hollow cone atomizer. The major findings from this work are as follows.

(1) Systematic experiments indicate that the regimes of instability for the three swirlers do not occur for the same chamber length and that they also differ in peak frequency and limit cycle amplitude levels.

(2) The determination of the FDF undertaken in a second stage raises important issues. For injectors that are weakly transparent to acoustic waves, it is shown that it is not advisable to determine the FDF from the velocity fluctuations measured in the plenum upstream of the swirler. It is found preferable to measure the velocity fluctuations at the injector outlet, at the base of the flame. However, the incoming disturbances ensuing from a swirling injector are nonuniform at the outlet section. It is then essential to find the optimal location for measuring the relative velocity fluctuations. It is shown that this choice is critical and that for the swirling injectors considered in the present study, this location is found to be close to the peak of mean velocity. The question on the validity of OH^* chemiluminescence as a heat release rate indicator is also analyzed in detail. It is found that for the spray flames considered here, the equivalence ratio fluctuations are small compared to the velocity fluctuations. This is attributed to the recessed position of the atomizer with respect to the backplane, which causes a part of the fuel spray to fluctuate in phase with the flow of air inside the injector, and high volatility of the fuel used.

(3) Systematic measurements indicate that the phase of FDF is relatively insensitive to the amplitude level but that the phase curves corresponding to the three swirlers are distinct. The gain of FDF remains in the linear regime even up to a fluctuation levels of 35% for two of the swirlers having the same swirl number and different pressure losses. For the swirler with the highest value of swirl number and pressure drop, the

gain changes substantially with the fluctuation level beyond 500 Hz but remains in the linear regime in the low frequency range.

(4) It is next indicated that the standard modeling approach that uses acoustically coupled cavities in closed-open conditions cannot explain the observed instability regimes. In the case of injection units which have a significant pressure drop and are therefore acoustically weakly transparent, it is necessary to represent the injector outlet with a specific impedance. A low-order modeling approach combining measured injector impedances and flame describing functions (FDFs) can then be used to explain the experimentally observed behavior and obtain an estimate for the growth rate and frequency of instability. The instability bands deduced from this model markedly differ from the classical ranges $[\pi, 2\pi] \bmod 2\pi$ by an offset of more than $\pi/2$. By further combining the model with damping rate estimates, predictions can also be derived for limit cycle amplitudes.

In summary:

- The injector imposes a specific impedance at the chamber inlet which displaces the bands of instability in a way that depends on the swirler characteristics.
- It defines the flame geometry and its dynamics and this is reflected in changes in the FDF gain and phase functions. These changes together with those observed in the injector impedance determine whether an operating point belongs to a band of instability.
- It contributes to the damping rate. The levels induced by the different swirlers and deduced from resonance experiments under cold flow conditions change and the relative difference between injectors may reach up to 20%. The cold flow damping rates are, however, found to be a fraction of those estimated under hot fire conditions using an energy balance method.

The admittedly simplified modeling approach highlights the importance of injector impedance on stability and allows to retrieve most but not all of the instability features observed in the systematic experiments described in this article.

Acknowledgments

The authors wish to thank the reviewers for their many helpful comments and suggestions. This work was partially supported by SafranTech (contract NF5Z-5100), by project FASMIC ANR16-CE22-0013 of the French National Research Agency (ANR), and by the European Union's Horizon 2020 research and innovation programme Annulight, with grant agreement no. 765998.

Appendix A. Phase evolution with the location of the velocity measurement point

It is interesting to see how the phase of velocity disturbances evolves as a function of the radial position. This is accomplished by acquiring the velocity signal delivered by the LDA system together with a reference signal constituted by the generator waveform delivered to the power amplifier. The phase between these two signals is plotted as a function of the radial distance to the injector axis radii in Fig. A.16. This figure also shows the mean flow velocity measured under cold flow conditions (the corresponding profile is the same as that appearing in Fig. 5a $\bar{u}_{c,r}$). The flow is modulated at 700 Hz and at an amplifier voltage of 3 V. It can be seen that the phase is only roughly constant in the region where the velocity fluctuations are being measured for FDF (between 3 mm to 4 mm). It also features rapid changes outside that region. This makes it necessary to account for this phase shift as a function of the radius in calculating the volumetric flow rate fluctuation. This also indicates that the optimal point for measuring velocity modulations is in the region where the phase variation is minimal (in the present case, between 3 and 4 mm from the injector axis).

The phase evolution taken into account in the calculation of the integrated volume flow rate is shown in Fig. 7.

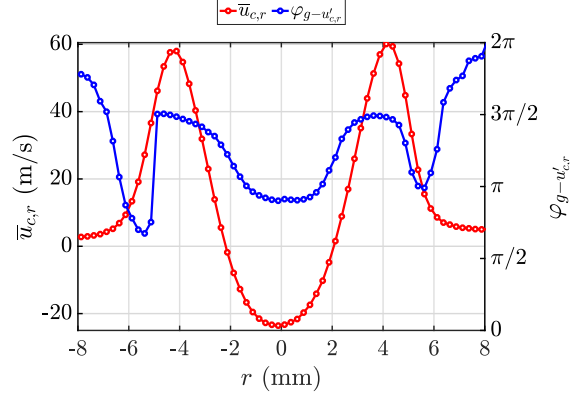


Figure A.16: Mean velocity profile (red) and phase between generator signal and velocity fluctuations (blue). These measurements are made under cold conditions with oil seeding and by modulating the system at 700 Hz and $V_0 = 3$ V. The measurements are performed at a height of $h = 2.5$ mm above the chamber backplane.

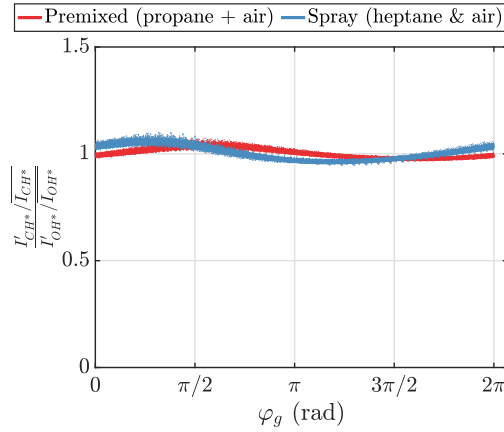


Figure B.17: I_{CH^*}/I_{OH^*} ratio (normalized by their respective mean) between perfectly premixed propane (red) and heptane spray flame (blue) as a function of wave generator's phase φ_g . Results are shown for the swirler 716 pulsed at 500 Hz and for an amplifier voltage of $V_0 = 3$ V.

Appendix B. Evolution of the I_{CH^*}/I_{OH^*} ratio during an oscillation cycle

A question that is often raised is whether flame chemiluminescence from OH^* radicals can be used as a heat release rate indicator for technically premixed flames. It is generally admitted that the OH^* signal can be used for premixed flames with a constant equivalence ratio. In the present case of a spray flame, one may expect that the equivalence ratio will vary, and that this will influence the chemiluminescence signal. It is then logical to compare these two cases. It is known for hydrocarbon flames that the equivalence ratio can be linked to the light intensity ratio I_{CH^*}/I_{OH^*} [32, 33, 34, 35]. This ratio normalized by the mean value is determined here for several conditions considered in this study: for the three swirlers (707, 712, and 716), for different amplitudes of modulation (0.5 V to 3.5 V), and for the frequency range of interest. The light intensities are recorded with two photomultipliers equipped with interference filters CH^* (430 nm with a width of 10 nm) and OH^* (308 nm with a width of 10 nm) placed side by side to capture the light from the entire flame. The data are recorded for a period of 2 s at a rate of 16,384 Hz. The signal from the wave generator (delivered to the driver units) is recorded simultaneously with the photomultiplier signals. Figure B.17 displays the light intensity ratio for 716 during a cycle at 500 Hz for an amplifier voltage of 3 V (peak to peak) as a function of the wave generator's phase φ_g . It is worth noting that the

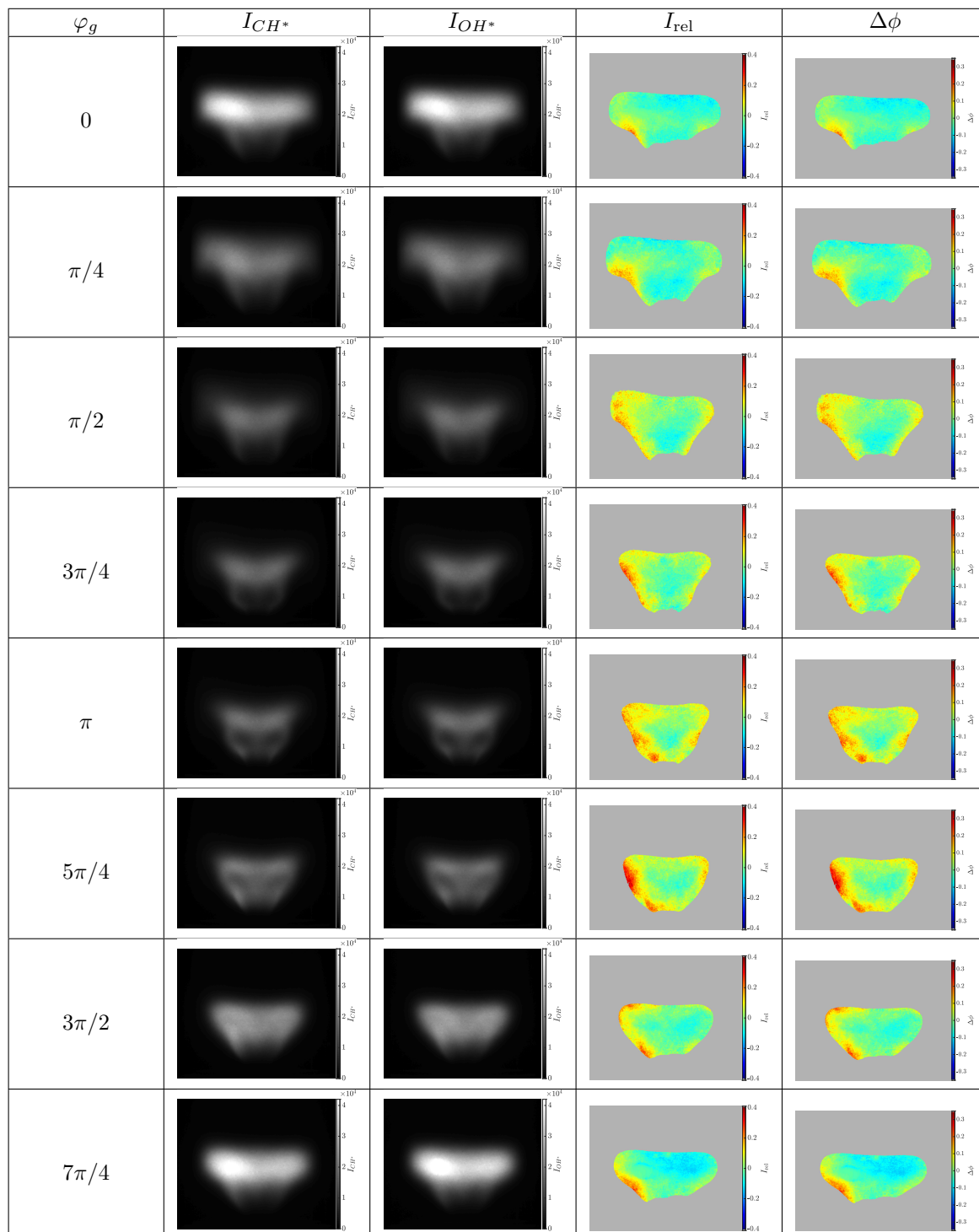
ratio of instantaneous intensities is scaled by the ratio of mean intensities so that the gains of the two photomultipliers do not intervene. A dispersion of the points around an average value can be observed but this is quite small. There is a ripple in the light intensity ratio during the oscillation cycle reaching about 10% of the average value. This variation during the cycle may reflect a variation in the equivalence ratio due to the air flow modulation, but it can also be linked to variations in dilution that are found in confined premixed flames when they are subjected to cyclic oscillations. This is because the fresh reactants entrain an amount of burnt gases from the outer recirculation zone. This is illustrated by examining the light intensity ratio in the same geometrical configuration but for a flame that is fully premixed. Mixing between air and propane is achieved far upstream in the air line. In this experiment the spray atomizer is inoperative and the flame has a color and shape similar to the spray flame (shown in [53]). A small variation in $(I(\text{CH}^*)/I(\text{OH}^*)) / (\overline{I(\text{CH}^*)} / \overline{I(\text{OH}^*)})$ can be observed in the premixed case as well, at certain instants of the cycle. The ripple during the acoustic cycle is of the same order of magnitude as for the spray flame. The measurements performed with the other swirlers at other frequencies and amplitudes yield similar results. This confirms that the spray flame essentially behaves like a premixed flame with a level of equivalence ratio variations that is small compared to the flow fluctuations. The above measurements with photomultiplier still need to be validated to ensure the absence of any spatial equivalence ratio inhomogeneities. This is accomplished with an intensified CCD camera (PI-MAX from Princeton Instruments) equipped with CH^* and OH^* filters as in [36, 54]. Experiments are carried out at different phase instants of the generator signal while acoustically modulating the flame at 500 Hz. The first and second columns of Tab. B.3 show the chemiluminescence intensity with CH^* and OH^* filter respectively for the heptane spray flame. A filtering operation is performed on the raw images to only retain the portions that contain at least 20% of the maximum intensity at each phase instant. As seen from the chemiluminescence images, the intensity distribution does not vary much between the two quantities. Next, the relative intensity deviation I_{rel} of the local to the mean intensity averaged over the oscillation cycle, calculated using Eq. B.1, is presented in the third column of Tab. B.3.

$$I_{\text{rel}} = \left[\frac{I_{\text{CH}^*}^{x,z}}{I_{\text{OH}^*}^{x,z}} - \frac{\overline{I_{\text{CH}^*}^{x,z}}}{\overline{I_{\text{OH}^*}^{x,z}}} \right] / \left[\frac{\overline{I_{\text{CH}^*}^{x,z}}}{\overline{I_{\text{OH}^*}^{x,z}}} \right] \quad (\text{B.1})$$

The deviation is minor, mostly less than 10% in the flame zone, except in small regions close to the periphery where the deviation is slightly higher (the captured light intensity is also smaller in these regions). To obtain the value of equivalence ratio ϕ from the flame images, a calibration of $I_{\text{CH}^*} / I_{\text{OH}^*}$ with equivalence ratio is performed under steady conditions. During these measurements, the fuel flow rate is maintained constant to ensure even atomization quality, and the air flow rate is varied to obtain different equivalence ratios. Figure B.18 shows the variation of spatially averaged $\overline{I_{\text{CH}^*}^{x,z}} / \overline{I_{\text{OH}^*}^{x,z}}$ with ϕ at different levels of fuel flow rate. It is to be noted that, when operating at lower fuel flow rates, the flame is not well stabilized at $\phi < 0.7$, and the measurements are less reliable. However, in the present case, the combustor is operated at $\phi = 0.85$ and $\dot{m}_f = 0.52 \text{ kg h}^{-1}$ where the data quality is adequate, and the slope is nearly linear between $\phi = 0.8$ and 1. The relationship between the intensity ratio and equivalence ratio is obtained using this calibration curve and is found to be $\Delta \overline{I_{\text{CH}^*}^{x,z}} / \overline{I_{\text{OH}^*}^{x,z}} \approx 1.17 \Delta \phi$ at $\dot{m}_f = 0.52 \text{ kg h}^{-1}$. The spatial evolution of relative equivalence ratio obtained using this relation shown in the fourth column of Tab. B.3 indicates that the spatial variation of equivalence ratio in the flame is small and that there is no visible stratification. From these results, a relative global equivalence ratio fluctuation $\Delta \phi_{gl} / \bar{\phi}$ (where $\bar{\phi} = 0.85$) can be obtained and is equal to 0.04, much lower than the relative velocity fluctuation of $u'_{c,r} / \bar{u}_{c,r} = 0.22$ at this frequency. This result is similar to the observation reported by [36] for a kerosene spray flame having negligible equivalence ratio fluctuation compared to velocity fluctuation. Furthermore, as observed by [55] through numerical simulation of a V-flame, any fluctuation in equivalence ratio would also result in velocity fluctuations. The above measurement is also performed at 700 Hz and similar results are obtained. Although strong variation in equivalence ratio could normally be expected in a spray flame, the reason for finding only minor fluctuations can be attributed to the recessed location of the fuel atomizer inside the injector and high volatility of the fuel used. Because of the recessed position, a part of the fuel spray impinges on the converging cone of the terminal plate (Fig. 1a) before being fully atomized. This part of the fuel spray can be expected to undergo fluctuations in flow rate along with the air, as observed by [56] through LES simulations on a similar injector. This could

be thought to reduce the fluctuation in equivalence ratio compared to a case where the fuel is conveyed directly into the chamber without any impact. In that case, any fluctuation in air flow rate would indeed change the equivalence ratio. This argument is validated by performing measurements at a smaller atomizer recess distance against the nominal recess distance of 6.75 mm from the backplane. This arrangement would prevent the fuel spray from impacting the convergent cone, and the spray will be delivered directly into the combustion chamber. One observes in this case that the relative I_{OH^*}/I_{CH^*} ratio indeed exhibits a higher deviation than at the nominal recess distance, substantiating the previous interpretation. The results for the smaller recess distance are not shown here and are to be presented in a future article. The weak equivalence ratio fluctuation observed in the present case is also demonstrated through numerical simulations performed with a similar injector geometry in [57]. One may therefore assume for the present spray flame case, as for the premixed flames, that the light intensity of OH^* is indicative of the heat release rate integrated over the flame volume \dot{Q} .

Table B.3: OH*, CH*, relative intensity deviation, and equivalence ratio deviation for heptane spray flame with swirler 716 measured when the flame is acoustically forced at 500 Hz and $V_0 = 3 \text{ V}$ ($u'_{c,r}/\bar{u}_{c,r} = 0.22$) at different phase instants φ_g of the reference generator signal. The fuel flow rate is 0.52 kg h^{-1} and the global equivalence ratio is 0.85.



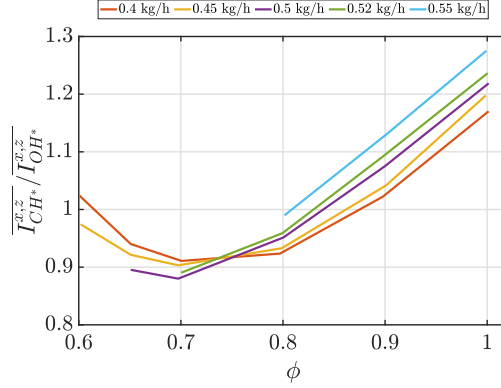


Figure B.18: Variation of mean CH^*/OH^* ratio with respect to equivalence ratio ϕ at different levels of fuel flow rate performed under steady conditions. The spatially resolved measurements are performed with an intensified CCD camera and the mean of the flame image at each operating point is calculated to obtain $\overline{I_{CH^*,z}^{x,z}}/\overline{I_{OH^*}^{x,z}}$. The measurements are performed with swirler 716.

Appendix C. Injector dynamics during SSO and acoustic forcing

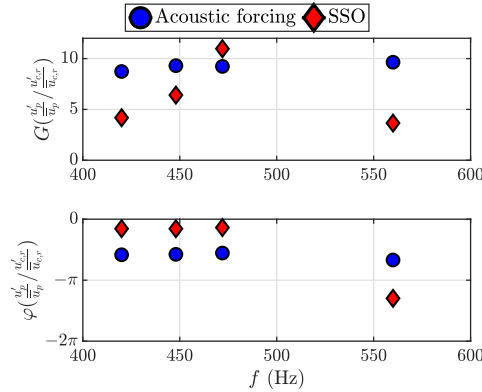


Figure C.19: The gain and phase of relative plenum velocity fluctuations to relative chamber velocity fluctuations at different frequencies during SSO and acoustic forcing. The results are shown when the chamber velocity fluctuations during an acoustic modulation are almost the same as SSO.

The measurements carried out in this work are now used to compare the velocity fluctuations upstream and downstream of the injector during an SSO and when the system is acoustically modulated. The velocity fluctuation upstream of the injector u_p' , is determined by the two-microphone method using pressure signals from microphones MP1 and MP3 mounted on the plenum (refer Fig. 1b). Downstream of the injector, the velocity fluctuation $u_{c,r}'$ is obtained by LDA at the nominal location discussed in Section 4.2. Experiments during an acoustic modulation were performed such that the velocity fluctuation was close to that found in the SSO case. The gain and phase of the relative fluctuations are shown in Fig. C.19. Significant differences can be observed in the gain between the SSO and the acoustically modulated case, with the difference being twice as much at certain frequencies. The phase between the upstream and downstream velocity signals (Fig. C.19 bottom) is also quite different between the two cases. In the forced case, the phase shift is slightly greater than $\pi/2$, and roughly independent of the frequency. In the SSO case, the phase shift is almost zero for low frequencies and close to π at 560 Hz. These results clearly show that the injector does not have the same behavior in the two cases: during acoustic forcing and under SSO. The injectors considered in this

study are weakly transparent to acoustic waves and present a significant pressure drop with abrupt area changes inside the swirler channels. It is thus not advisable to evaluate the FDF from velocity measurements performed in the plenum. The traditional modeling approach based on $[\pi, 2\pi] \bmod 2\pi$ instability bands also ceases to work for such injectors.

References

- [1] D. J. Harrje, F. H. Reardon, Liquid propellant rocket combustion instability, Tech. Rep. No. SP-194, NASA Headquarters Washington, DC, USA, 1972.
- [2] V. Yang, W. Anderson, Liquid Rocket Engine Combustion Instability, Am. Inst. Aeronaut. Astronaut., 1995.
- [3] S. Candel, Combustion dynamics and control: Progress and challenges, Proc. Combust. Inst. 29 (2002) 1–28.
- [4] Y. Huang, V. Yang, Dynamics and stability of lean-premixed swirl-stabilized combustion, Prog. Energy Combust. Sci. 35 (2009) 293–364.
- [5] T. Poinsot, Prediction and control of combustion instabilities in real engines, Proc. Combust. Inst. 36 (2017) 1–28.
- [6] Y. Méry, Dynamical response of a perfectly premixed flame and limit behavior for high power density systems, Combust. Flame 192 (2018) 410–425.
- [7] A. M. Steinberg, I. Boxx, M. Stöhr, C. D. Carter, W. Meier, Flow–flame interactions causing acoustically coupled heat release fluctuations in a thermo-acoustically unstable gas turbine model combustor, Combust. Flame 157 (2010) 2250–2266.
- [8] A. M. Steinberg, C. M. Arndt, W. Meier, Parametric study of vortex structures and their dynamics in swirl-stabilized combustion, Proc. Combust. Inst. 34 (2013) 3117–3125.
- [9] N. Syred, A review of oscillation mechanisms and the role of the precessing vortex core (PVC) in swirl combustion systems, Prog. Energy Combust. Sci. 32 (2006) 93–161.
- [10] S. Candel, D. Durox, T. Schuller, J.-F. Bourgoquin, J. P. Moeck, Dynamics of swirling flames, Annu. Rev. Fluid Mech. 46 (2014) 147–173.
- [11] C. Stone, S. Menon, Swirl control of combustion instabilities in a gas turbine combustor, Proc. Combust. Inst. 29 (2002) 155–160.
- [12] Y. Huang, V. Yang, Effect of swirl on combustion dynamics in a lean-premixed swirl-stabilized combustor, Proc. Combust. Inst. 30 (2005) 1775–1782.
- [13] D. Durox, J. P. Moeck, J.-F. Bourgoquin, P. Morenton, M. Viallon, T. Schuller, S. Candel, Flame dynamics of a variable swirl number system and instability control, Combust. Flame 160 (2013) 1729–1742.
- [14] K. T. Kim, Combustion instability feedback mechanisms in a lean-premixed swirl-stabilized combustor, Combust. Flame 171 (2016) 137–151.
- [15] T. Schuller, D. Durox, P. Palies, S. Candel, Acoustic decoupling of longitudinal modes in generic combustion systems, Combust. Flame 159 (2012) 1921–1931.
- [16] G. Vignat, D. Durox, K. Prieur, S. Candel, An experimental study into the effect of injector pressure loss on self-sustained combustion instabilities in a swirled spray burner, Proc. Combust. Inst. 37 (2019) 5205–5213.
- [17] W. Polifke, A. Fischer, T. Sattelmayer, Instability of a premix burner with nonmonotonic pressure drop characteristic, J. Eng. Gas Turbines Power 125 (2003) 20–27.
- [18] G. Vignat, D. Durox, T. Schuller, S. Candel, Combustion dynamics of annular systems, Combust. Sci. Tech. 192 (2020) 1358–1388.
- [19] A. Fischer, C. Hirsch, T. Sattelmayer, Comparison of multi-microphone transfer matrix measurements with acoustic network models of swirl burners, J. Sound Vib. 298 (2006) 73–83.
- [20] A. P. Dowling, Nonlinear self-excited oscillations of a ducted flame, J. Fluid Mech. 346 (1997) 271–290.
- [21] N. Noiray, D. Durox, T. Schuller, S. Candel, A unified framework for nonlinear combustion instability analysis based on the flame describing function, J. Fluid Mech. 615 (2008) 139–167.
- [22] G. Vignat, P. Rajendram Soundararajan, D. Durox, A. Vié, A. Renaud, S. Candel, A joint experimental and les characterization of the liquid fuel spray in a swirl injector, J. Eng. Gas Turbines Power 143 (2021) 081019.
- [23] G. Vignat, Injection and combustion dynamics in swirled spray flames and azimuthal coupling in annular combustors, Ph.D. thesis, CentraleSupélec, University Paris-Saclay, Gif sur Yvette, France (2020).
- [24] R. Gaudron, Acoustic response of premixed flames submitted to harmonic sound waves, Ph.D. thesis, CentraleSupélec, University Paris-Saclay, Gif sur Yvette, France (2018).
- [25] D. Durox, S. Ducruix, F. Lacas, Flow seeding with an air nebulizer, Exp. Fluids 27 (1999) 408–413.
- [26] D. Ebi, A. Denisov, G. Bonciolini, E. Boujo, N. Noiray, Flame dynamics intermittency in the bistable region near a subcritical hopf bifurcation, J. Eng. Gas Turbines Power 140 (2018) 061504.
- [27] P. Baade, Combustion oscillations in gas-fired appliances, Proc. Second AGA/IGT Conf. Nat. Gas Res. Technol. (1972) paper 1.
- [28] V. Goldschmidt, R. Leonard, J. Riley, G. Wolfbrandt, P. Baade, Transfer function of gas flames: method of measurement and representative data, ASHRAE Trans. (1978) 466–476.
- [29] I. R. Hurler, R. B. Price, T. M. Sugden, A. Thomas, Sound emission from open turbulent premixed flames, Proc. R. Soc. London Series a-Math. Phys. Sci. 303 (1968) 409–427.
- [30] J. Ballester, T. Garcia-Armingol, Diagnostic techniques for the monitoring and control of practical flames, Prog. Energy Combust. Sci. 36 (2010) 375 – 411.
- [31] C. Mirat, D. Durox, T. Schuller, Analysis of the spray and transfer function of swirling spray flames from a multi-jet steam assisted liquid fuel injector, ASME Turbo Expo: Power for Land, Sea, and Air (2014) paper GT2014–25111.

- [32] J. Kojima, Y. Ikeda, T. Nakajima, Spatially resolved measurement of OH*, CH*, and C2* chemiluminescence in the reaction zone of laminar methane/air premixed flames, *Proc. Comb. Inst.* 28 (2000) 1757–1764.
- [33] N. Docquier, S. Candel, Combustion control and sensors: a review, *Prog. Energy Combust. Sci.* 28 (2002) 107–150.
- [34] M. Orain, Y. Hardalupas, Effect of fuel type on equivalence ratio measurements using chemiluminescence in premixed flames, *C. R. Mécanique* 338 (2010) 241–254.
- [35] Y. Ding, D. Durox, N. Darabiha, T. Schuller, Combustion state monitoring of premixed heating appliances with flame ionization current and chemiluminescence, *Combust. Sci. Technol.* 191 (2019) 382–401.
- [36] M. Vogel, M. Bachfischer, J. Kaufmann, T. Sattelmayer, Experimental investigation of equivalence ratio fluctuations in a lean premixed kerosene combustor, *Exp. Fluids* 62 (2021) 1–14.
- [37] B. Schuermans, F. Guethe, W. Mohr, Optical transfer function measurements for technically premixed flames, *J. Eng. Gas Turbines Power* 132 (2010) 081501.
- [38] S. Bade, M. Wagner, C. Hirsch, T. Sattelmayer, B. Schuermans, Design for thermo-acoustic stability: modeling of burner and flame dynamics., *J. Eng. Gas Turbine Power* 135 (2013) 111502.
- [39] D. Durox, T. Schuller, S. Candel, Combustion dynamics of inverted conical flames, *Proc. Combust. Inst.* 30 (2005) 1717–1724.
- [40] K. Prieur, Dynamique de la combustion dans un foyer annulaire multi-injecteurs diphasique, Ph.D. thesis, Université Paris-Saclay, prepared at CentraleSupélec, Gif-sur-Yvette, France (2017).
- [41] G. Staffelbach, L. Y. M. Gicquel, G. Boudier, T. Poinsot, Large Eddy Simulation of self excited azimuthal modes in annular combustors, *Proc. Combust. Inst.* 32 (2009) 2909–2916.
- [42] C. Patat, F. Baillot, J.-B. Blaisot, E. Domingues, Responses of lean swirling spray flames to acoustic pressure and transverse velocity perturbations, *Symposium on Thermoacoustics in Combustion: Industry meets Academia (SoTiC)* (2021) paper 8499.
- [43] F. Baillot, F. Lespinasse, Response of a laminar premixed V-flame to a high-frequency transverse acoustic field, *Combust. Flame* 161 (2014) 1247–1267.
- [44] J. O’Connor, V. Acharya, T. Lieuwen, Transverse combustion instabilities: Acoustic, fluid mechanic, and flame processes, *Prog. Energy Combust. Sci.* 49 (2015) 1–39.
- [45] J. Hutt, M. Rocker, High-Frequency injection-coupled combustion instability, in: V. Yang, W.E. Anderson (Eds.), *Liquid Rocket Engine Combustion Instability*, Am. Inst. Aeronaut. Astronaut., 1995.
- [46] D. Durox, T. Schuller, N. Noiray, A. L. Birbaud, S. Candel, Rayleigh criterion and acoustic energy balance in unconfined self-sustained oscillating flames, *Combust. Flame* 156 (2009) 106–119.
- [47] T. Schuller, T. Poinsot, S. Candel, Dynamics and control of premixed combustion systems based on flame transfer and describing functions, *J. Fluid Mech.* 894 (2020) 1–95.
- [48] S. Rienstra, A. Hirschberg, An introduction to acoustics, Report IWDE 92-06, Eindhoven University of Technology, 2004.
- [49] J.-F. Bourgouin, Dynamique de flamme dans les foyeres annulaires comportant des injecteurs multiples, Ph.D. thesis, Ecole Centrale de Paris, France (2014).
- [50] T. Poinsot, D. Veynante, *Theoretical and numerical combustion*, R.T. Edwards Inc., 2012.
- [51] N. Noiray, D. Durox, T. Schuller, S. Candel, A Method for Estimating the Noise Level of Unstable Combustion Based on the Flame Describing Function, *Int. J. Aeroacoustics* 8 (2009) 157–176.
- [52] K. Prieur, D. Durox, T. Schuller, S. Candel, Strong azimuthal combustion instabilities in a spray annular chamber with intermittent partial blow-off, *J. Eng. Gas Turbines Power* 140 (2018) 031503.
- [53] P. Rajendram Soundararajan, G. Vignat, D. Durox, A. Renaud, S. Candel, Effect of different fuels on combustion instabilities in an annular combustor, *J. Eng. Gas Turbines Power* 143 (2021) 031007.
- [54] D. Guyot, F. Guethe, B. Schuermans, A. Lacarelle, C. O. Paschereit, CH*/OH* chemiluminescence response of an atmospheric premixed flame under varying operating conditions, *ASME Turbo Expo: Power for Land, Sea, and Air* (2010) paper GT2010-23131.
- [55] A.-L. Birbaud, S. Ducruix, D. Durox, S. Candel, The nonlinear response of inverted “V” flames to equivalence ratio nonuniformities, *Combust. Flame* 154 (2008) 356–367.
- [56] E. L. Schiavo, D. Laera, E. Riber, L. Gicquel, T. Poinsot, Effects of liquid fuel/wall interaction on thermoacoustic instabilities in swirling spray flames, *Combust. Flame* 219 (2020) 86–101.
- [57] G. Vignat, E. L. Schiavo, D. Laera, A. Renaud, L. Gicquel, D. Durox, S. Candel, Dynamics of spray and swirling flame under acoustic oscillations: A joint experimental and LES investigation, *Proc. Combust. Inst.* 38 (2021) 6015–6024.